University of Tehran Press

Journal of the Earth and Space Physics
Homepage: https://jesphys.ut.ac.ir

Vol. 51, No. 4, Winter 2026, P. 233-263

(Research Article)

Teleconnection Drivers of Extreme Precipitation over Iran: A Causal-Network Perspective (1980–2024)

Saadat Moghadasi, A. R. ✉

Department of Irrigation and Reclamation Engineering, Faculty of Agriculture, College of Agriculture and Natural Resources, University of Tehran, Karaj, Iran.

Corresponding Author E-mail: saadatmoghadasi28@ut.ac.ir

(Received: 7 Jan 2026, Revised: 12 Feb 2026, Accepted: 24 Feb 2026, Published online: 17 March 2026)

Abstract

This study provides a quantitative and process-oriented assessment of how large-scale ocean–atmosphere teleconnection patterns modulate extreme precipitation over Iran during 1979–2024. Using daily observations from 160 synoptic stations, precipitation extremes were characterized through ETCCDI indices (R10mm, R20mm, R95p, Rx5day), seasonal totals, and SPI-3, and subsequently aggregated into five quasi-homogeneous hydro-climatic clusters. A causal discovery framework based on the PCMCI+ algorithm was employed to infer directed and lagged relationships between twelve major teleconnection indices and regional precipitation metrics. Network diagnostics reveal a pronounced asymmetry between drivers and responses: teleconnection nodes exhibit higher total degree (≈19.3 ± 10.2) and betweenness centrality (≈0.07 ± 0.08) than precipitation nodes, confirming their dominant large-scale control. ENSO-related indices (Niño-3.4, ONI, MEI, SOI) jointly account for nearly 65% of the aggregated absolute causal strength over southern Iran, followed by the Indian Ocean Dipole (≈13%) and EAWR (≈10%). Short-duration intensity metrics (Rx1day and Rx5day) display the strongest cumulative teleconnection influence (exceeding 33% of the total signal), whereas moderate wet-day frequencies show weaker connectivity. Seasonally, robust links are concentrated in SON and MAM, with dynamically consistent and statistically supported signals also emerging in DJF, while JJA remains comparatively weakly connected. Composite analyses of upper-tropospheric wind at 250 hPa, mid-tropospheric geopotential height at 500 hPa (Z500), and lower-tropospheric moisture transport at 850 hPa indicate that teleconnections primarily act through reorganization of the subtropical and mid-latitude jet streams, modulation of Rossby wave-train structure, and alteration of mid-level baroclinicity and low-level moisture convergence. Overall, the results demonstrate that extreme precipitation over Iran is governed by a limited set of dynamically efficient teleconnections whose influence is seasonally modulated and regionally heterogeneous. These findings provide a quantitative basis for improving seasonal predictability and for evaluating process representation in climate-model simulations.

Keywords: Teleconnection indices, Pacific Ocean, East Atlantic, Exorbitant New Method.

1. Introduction

Heavy precipitation and hydrological extremes have intensified in many regions of the world under ongoing global warming, with robust evidence for increases in the frequency and intensity of sub-daily to multi-day rainfall extremes in a warming climate (IPCC, 2021). Over semi-arid and arid regions, such as the Middle East and North Africa, this intensification co-exists with long-term drying trends, leading to a paradoxical combination of more frequent droughts and more hazardous short-lived flood events. Iran located at the intersection of several major storm tracks and subtropical subsidence zones and is therefore exceptionally sensitive to shifts in large-scale circulation, moisture transport pathways and remote modes of variability.

A growing body of research shows that teleconnection patterns – including the El Niño–Southern Oscillation (ENSO), the Indian Ocean Dipole (IOD), the North Atlantic and Arctic Oscillations (NAO and AO), and North Pacific modes such as the Pacific Decadal Oscillation (PDO), and the Atlantic Multidecadal Oscillation (AMO) – modulate precipitation over the Middle East on interannual to decadal time scales (Rezaei, 2021; Mahbod et al., 2023; Nuroozi et al., 2025). For Iran, these modes influence both the strength and position of the Mediterranean storm track, the subtropical jet

Cite this article: SaadatMoghadasi, A. R., (2026). Teleconnection Drivers of Extreme Precipitation over Iran: A Causal-Network Perspective (1980–2024). *Journal of the Earth and Space Physics*, 51(4), 233-263. DOI: http//doi.org/10.22059/jesphys.2026.408553.1007744

Publisher: University of Tehran Press.
DOI: http//doi.org/10.22059/jesphys.2026.408553.1007744

Print ISSN: 2538-371X
Online ISSN: 2538-3906

and Red Sea and Persian Gulf moisture plumes, with demonstrable impacts on seasonal rainfall totals and the occurrence of persistent droughts (Aghelpour et al., 2023; Afsari et al., 2024). However, most existing studies rely on correlation or regression techniques that treat individual teleconnections separately and typically consider only basin-averaged precipitation, offering limited insight into spatial contrasts or into the directionality of influence among multiple drivers.

Recent analyses of Iranian precipitation extremes have highlighted strong regional contrasts in the response of wet and dry spells to large-scale circulation. For example, Mahbod et al. (2023) documented significant teleconnection control on the frequency of wet and dry spells across Iran, while Jamshidi Khezeli et al. (2022) demonstrated that specific combinations of ENSO, NAO and Madden–Julian Oscillation (MJO) phases regulate autumn and winter extreme precipitation events over western Iran. At the same time, compound indices of drought and heavy rainfall in Iranian cities reveal a tendency towards more frequent very heavy precipitation days and longer dry spells in future climate projections (Afsari et al., 2024). These findings collectively suggest that changes in remote drivers can reorganize the spatial pattern of extremes, yet the structure of that teleconnection network has not been quantified in a unified framework.

Beyond the Middle East, a number of recent studies have begun to examine precipitation extremes through a multi-driver lens, often using teleconnection indices as predictors of regional flood or drought risk (Hussain *et al.,* 2023; Wang et al., 2025; Ntawuruhunga et al., 2025). Such studies emphasize that local extremes are rarely controlled by a single mode of variability; instead, they emerge from the interaction of several partially coherent climate patterns acting at different time scales. Network-based perspectives and causal discovery methods are therefore increasingly advocated as tools to disentangle the relative roles of competing drivers and to move beyond purely associative analyses (Tibau et al., 2022; Galytska et al., 2023; Miersch et al., 2025; Runge et al., 2023).

Temporal harmonization: To ensure methodological consistency across variables, all teleconnection indices and hydroclimatic predictors were harmonized to a common seasonal timescale prior to causal discovery. Daily precipitation fields were first summarized into ETCCDI-style seasonal indices (with Rx5day as the primary extreme metric analyzed), while monthly climate indices were aggregated to matching seasonal means. Accordingly, all inputs to PCMCI+ share the same temporal resolution, allowing conditional independence testing to be interpreted consistently across nodes. Although several ETCCDI-style indices are analyzed to characterize intensity and frequency dimensions of extreme precipitation, Rx5day is treated as the primary extreme metric in the causal-network analysis. This choice reflects its ability to capture multi-day storm persistence and accumulated synoptic-scale rainfall, which are dynamically more consistent with teleconnection-driven circulation anomalies than single-day extremes (e.g., Rx1day).

Justification of teleconnection indices: The selected teleconnection set was designed to represent the dominant modes of tropical variability (ENSO family; Niño-3.4/ONI/MEI/SOI), Indo-Pacific forcing, and key extratropical Atlantic–Eurasian patterns (e.g., AMO, NAO, AO, EAWR, and SCAND). While several indices reflect ENSO variability, they provide complementary views (SST-based vs. coupled atmosphere–ocean vs. pressure-based), and PCMCI+ further mitigates spurious dependencies by conditioning on the remaining network. Causal discovery algorithms such as PCMCI and PCMCI+ have been specifically developed for high-dimensional, autocorrelated geophysical time series, providing an avenue to infer directed, lagged links among teleconnection indices and regional hydroclimatic variables while controlling for confounding. These methods have already been applied to benchmark problems and to Arctic–midlatitude linkages, demonstrating their ability to recover known teleconnection pathways and to highlight non-trivial mediating processes to the best of our knowledge, no study has systematically applied a causal-network framework to quantify how an ensemble of ocean–atmosphere teleconnections controls spatio-temporal patterns of precipitation extremes over Iran.

In parallel, station-based analyses across Iran have revealed substantial heterogeneity in the behavior of extreme rainfall indices, with coastal, orographic and interior arid regions exhibiting sharply different trends in indices such as R10mm, R20mm, R95p and Rx5day, as well as in drought diagnostics including the Standardized Precipitation Index (SPI) (Nuroozi et al., 2025). Clustering stations into quasi-homogeneous rainfall regimes offers a compact representation of this heterogeneity, enabling a regionalized assessment of both long-term changes and sensitivity to remote forcings. However, most clustering studies stop at descriptive characterization and do not explicitly connect regional clusters to a multi-index teleconnection framework.

This study addresses these gaps by constructing a seasonally resolved, cluster-based description of extreme precipitation over Iran and embedding it in a causal network of major ocean–atmosphere teleconnections. Using daily precipitation records from 160 synoptic stations for 1979–2024, we derive a suite of ETCCDI-style extreme indices and SPI-based drought metrics for each station, cluster them into five robust rainfall regimes, and then build regional seasonal time series for each cluster. These regional series are analyzed jointly with twelve leading teleconnection indices – representing the tropical Pacific, Indian, and Atlantic oceans and the Northern Hemisphere extratropical circulation – using the PCMCI+ algorithm with lags up to one season. We finally track how the strength and topology of the teleconnection–extreme-precipitation network evolves between the late twentieth century and the early twenty-first century, thereby providing new evidence on the non-stationarity of teleconnection influences over a climatically sensitive region.

By combining high-resolution station data, a homogeneous-region clustering, and state-of-the-art causal discovery, the paper aims to (i) identify the dominant teleconnection controls on extreme precipitation indices in different parts of Iran; (ii) quantify preferred phase lags and the directionality of influence between remote modes and regional rainfall regimes; and (iii) diagnose structural changes in the teleconnection network between 1980–1999 and 2000–2024. The resulting causal maps highlight where and when ocean–atmosphere variability exerts the strongest leverage on extreme rainfall in Iran, offering a process-based basis for seasonal prediction and for evaluating climate model simulations of regional extremes.

2. Materials and Methods

2-1. Study area and precipitation data

The study domain comprises the entirety of Iran, spanning approximately 24–40°N and 44–63°E, and encompassing a wide variety of climatic regimes from the humid Caspian coastal plain to the high Zagros and Alborz ranges and the hyper-arid central plateaus. Daily precipitation data for 160 synoptic stations were obtained from the Islamic Republic of Iran Meteorological Organization (IRIMO) for the period January 1979 to December 2024. Stations were selected based on record length, continuity and basic quality-control criteria, requiring at least 95% data availability over the study period and minimal relocations. Quality control followed standard procedures, including range checks, internal consistency tests and comparison with neighboring stations, and suspicious values were either corrected using metadata or treated as missing.

2-1-1. Extreme precipitation and drought indices

To characterize rainfall extremes, a suite of indices consistent with the recommendations of the Expert Team on Climate Change Detection and Indices (ETCCDI) was calculated at the daily scale for each station. We focus on (i) R10mm, the number of days in a season with daily precipitation ≥ 10 mm; (ii) R20mm, the number of days with precipitation ≥ 20 mm; (iii) R95p, the seasonal total precipitation from days exceeding the station-specific 95th percentile of wet-day amounts during the 1990-2020 reference period; and (iv) Rx5day, the maximum 5-day accumulated precipitation within each season. In addition, the total seasonal accumulated precipitation was computed (Total Seasonal), and the Standardized Precipitation Index (SPI) was derived for a three-month accumulation window centered on each climatological season (SPI-3). SPI-3 was calculated by fitting a gamma distribution to seasonal precipitation totals and transforming the cumulative probabilities to a standard normal variate, yielding dimensionless anomalies that are comparable across regions and seasons. It is important to emphasize that SPI-3 represents background hydroclimatic conditions over a seasonal accumulation window rather than discrete extreme precipitation events. Accordingly, SPI-3 captures sustained wet or dry anomalies that may precondition extreme-event probability, but it should not be interpreted as a direct measure of short-duration rainfall extremes.

2-1-2. Seasonal aggregation and anomaly definition

Daily indices were first calculated on the native calendar and then aggregated to climatological seasons, defined as December–February (DJF), March–May (MAM), June–August (JJA) and September–November (SON). December values were assigned to the DJF season of the following calendar year, yielding four non-overlapping seasonal series per station and index. For each station and index, seasonal means and percentiles were computed over the 1990-2020 base period, and anomalies were defined as departures from the corresponding climatological mean. Before causal analysis, all seasonal time series were standardized to zero mean and unit variance, and where necessary, a linear trend was removed by ordinary-least-squares regression to emphasize interannual to decadal variability.

2-1-3. Regionalization by K-means clustering

To obtain quasi-homogeneous rainfall regimes, the 160 stations were clustered using K-means applied to a feature space combining long-term seasonal means of the extreme indices and total precipitation. Specifically, for each station we constructed a 20-dimensional vector comprising DJF, MAM, JJA and SON climatological means of R10mm, R20mm, R95p, Rx5day and Total Seasonal. Prior to clustering, each feature was standardized to zero mean and unit variance to prevent dominance by high-variance indices. The optimal number of clusters was determined by examining the silhouette coefficient, within-cluster sum of squares and the spatial coherence of the resulting regions, with K = 5 ultimately selected as a compromise between parsimony and the need to distinguish distinct coastal, orographic and interior regimes. The resulting clusters delineate (i) a humid Caspian coastal and Alborz-foothill region in the north, (ii) an orographic western and north-western Zagros domain, (iii) a south-western lowland region influenced by the Persian Gulf and Shatt-al-Arab/Khuzestan plains, (iv) an interior central plateau cluster, and (v) an eastern to south-eastern arid region.

For subsequent analyses, seasonal extreme indices and SPI-3 were averaged across all stations belonging to a given cluster, producing regional time series for each season and index. These cluster-mean series retain interannual to decadal variability while reducing local-scale noise and emphasizing coherent regional signals, as evidenced by the tight co-evolution of indices within each cluster.

2-1-4. Teleconnection indices

Twelve large-scale ocean–atmosphere modes of variability were considered as potential drivers of Iranian precipitation extremes: the Niño-3.4 sea-surface temperature index (NINO3.4), the Oceanic Niño Index (ONI) and the Southern Oscillation Index (SOI) for ENSO; the Dipole Mode Index for the Indian Ocean Dipole (DMI); the Atlantic Multidecadal Oscillation (AMO); the Pacific Decadal Oscillation (PDO); the North Atlantic Oscillation (NAO) and Arctic Oscillation (AO); the Scandinavian pattern (SCAND) and East Atlantic/Western Russia pattern (EAWR); the Multivariate ENSO Index (MEI); and the real-time multivariate MJO index aggregated to a single seasonal amplitude (MJO). Monthly values of these indices were obtained from operational climate data centers (primarily NOAA Climate Prediction Center, NOAA Physical Sciences Laboratory and the Japan Agency for Marine–Earth Science and Technology), and checked for consistency across overlapping data sets where available. The selection of teleconnection indices was guided by three complementary criteria: (i) physical relevance to Middle East hydroclimate, (ii) representation of distinct ocean–atmosphere sectors, and (iii) prior evidence of influence on Mediterranean–West Asia circulation. The final set therefore spans the dominant modes of tropical Pacific variability (ENSO family: Niño-3.4, ONI, MEI, and SOI), Indian Ocean forcing (IOD), Atlantic multidecadal variability (AMO), and key extratropical circulation patterns over the North Atlantic–Eurasian sector (NAO, AO, EAWR, and SCAND), as well as North Pacific variability (PDO). Together, these indices represent the principal large-scale modes known to modulate subtropical jet positioning, Mediterranean cyclogenesis, and moisture transport pathways into Iran. While some indices share partial dynamical ancestry (e.g., ENSO diagnostics), they provide complementary representations of coupled SST, atmospheric pressure, and multivariate variability. Importantly, the PCMCI+ framework conditions on all remaining nodes, thereby minimizing redundancy-driven spurious links and allowing the network to objectively identify the dynamically dominant drivers rather than presupposing them. While several ENSO-related indices are included (Niño-3.4, ONI, MEI, and SOI), they are not redundant diagnostics. Rather, they provide complementary representations of ENSO variability: SST-based (Niño-3.4, ONI), pressure-based (SOI), and coupled multivariate atmosphere–ocean diagnostics (MEI). The PCMCI+ framework further conditions on all remaining indices, thereby mitigating spurious links arising from shared ENSO ancestry. All teleconnection indices were converted to seasonal means or seasonal amplitude measures consistent with the DJF, MAM, JJA and SON definition used for precipitation. Seasonal values were then standardized to zero mean and unit variance over the common 1979–2024 period. To reduce potential aliasing between slow and fast components, low-frequency variability longer than 15 years was removed using a high-pass Butterworth filter in sensitivity tests; however, the primary results presented here rely on linearly detrended and standardized series without additional filtering.

2-1-5. Construction of seasonal multivariate data sets

For each climatological season, a multivariate time series data set was constructed by combining the twelve teleconnection indices with the cluster-mean precipitation metrics. Thus, for a given season and cluster, the analysis variables comprised the 12 teleconnection indices and, for precipitation, the regional time series of R10mm, R20mm, R95p, Rx5day, Total Seasonal and SPI-3. The resulting data matrices have length T = 46 years (1979–2024) and dimensionality up to 18 variables per season, suitable for application of modern causal discovery algorithms.

2-1-6. Causal discovery with PCMCI+

Directed and lagged dependencies among teleconnection indices and cluster-mean precipitation extremes were inferred using the PCMCI+ algorithm from the Tigramite package (Python). PCMCI+ combines a condition-selection step based on the PC algorithm with momentary conditional independence tests to estimate a sparse causal graph that is robust in the presence of strong autocorrelation and high dimensionality. Here, we employed the Par Corr test for primarily linear dependencies and verified key links with a kernel-based conditional mutual information test to capture potential nonlinearities. The maximum considered lag was set to one season (i.e. three months), corresponding to lag-0 and lag-1 seasonal relationships between teleconnections and precipitation indices; sensitivity experiments with a two-season lag confirmed that the majority of robust links are confined to lags ≤ 1 season.

For each season and cluster, PCMCI+ was applied to the standardized multivariate series with a significance level of 0.05, and false discovery rate control was used to account for multiple testing. Edges in the resulting causal graphs were weighted by the absolute value of the estimated partial correlation (for Par Corr) or by normalized conditional mutual information for the nonlinear test. From these weighted directed graphs we derived classic network metrics, including in-degree and out-degree, node strength and betweenness centrality, to quantify the relative influence of each teleconnection on regional extremes and the susceptibility of each cluster to remote forcing. The analysis was repeated separately for two sub-periods, 1980–1999 and 2000–2024, allowing assessment of structural changes in the teleconnection–precipitation network over time.

2-1-7. Comparison of early and recent periods

To diagnose potential non-stationarity in teleconnection influences, the PCMCI+ analysis was conducted independently for the late twentieth-century period (1980–1999) and the early twenty-first-century period (2000–2024). For each node, differences in out-strength and in-strength between the two periods were computed and visualized, along with changes in the sign and lag of the most important teleconnection–precipitation links. Particular attention was paid to changes in ENSO-, IOD- and MJO-related pathways towards the western and south-western clusters, where observational and modelling studies have suggested emerging shifts in moisture transport and storm-track behavior (Wang et al., 2025). These diagnostics provide a quantitative basis for discussing how anthropogenic climate change and internal variability may be reshaping the hierarchy of teleconnection controls on extreme precipitation over Iran. Because each sub-period contains fewer samples than the full 1979–2024 record, weaker teleconnection links are subject to increased sampling uncertainty. Therefore, structural comparisons focus primarily on robust, high-strength edges that persist across sensitivity experiments.

2-1-8. Data description

The station inventory comprises 160 synoptic stations distributed across Iran. For each station, geographic coordinates (latitude and longitude in degrees) and station elevation in meters relative to mean sea level (m a.s.l.) are provided. Elevation is emphasized here because it modulates near-surface temperature, orographic lifting, and the phase and intensity of cold-season precipitation.

2-1-9. Overall elevation statistics

Across all stations, elevation spans from -23.6 to 3747.0 m a.s.l. (range: 3770.6 m). The mean elevation is 1143.5 m and the median is 1284.8 m (interquartile range: 482.9 to 1657.3 m; standard deviation: 766.7 m). Six stations lie below sea level (southern Caspian lowlands), and 14 stations (8.8%) are located above 2000 m a.s.l.

2-1-10. Elevation class frequencies

Stations were grouped into broad altitude classes as follows (Table 1):

Table 1. Elevation-based classification of the synoptic stations investigated in this study.

Elevation class (m a.s.l.)	Number of stations
<0 m	6
0-500 m	36
500-1000 m	18
1000-1500 m	43
1500-2000 m	43
>2000 m	14

The highest-elevation station is Tochal (35.50°N, 51.05°E) at 3747.0 m a.s.l., representing the upper Alborz mountain environment. The lowest-elevation station is Anzali (37.28°N, 49.28°E) at -23.6 m a.s.l. Negative elevations are expected in parts of the southern Caspian basin.

2-1-11. Stations above 2000 m a.s.l.

14 stations exceed 2000 m a.s.l. These sites are primarily associated with the Alborz and Zagros highlands and are likely to experience stronger orographic enhancement and colder winter conditions than lowland stations.
Table 2 depicts their characteristics.

Table 2. List of stations above 2000 m a.s.l.

Rank	Station	Latitude (°N)	Longitude (°E)	Elevation (m a.s.l.)
1	Tochal	35.50	51.05	3747.0
2	Disen Bala	36.04	51.47	3328.0
3	Alovares	38.92	47.56	3056.0
4	Ferydoon Shahr	32.94	50.12	2490.0
5	Abali	35.76	51.96	2465.2
6	Menshad	31.53	54.22	2346.0
7	Eghlyied	30.53	52.68	2300.0
8	Rabar	29.29	56.91	2285.0
9	Baft	29.23	56.59	2280.0
10	Mygoon	35.44	51.44	2270.0
11	Sepidan	30.16	51.59	2201.0
12	Astyan	34.52	50.00	2097.0
13	Sahrekord	32.22	50.86	2054.3
14	Damavand	35.57	52.06	2051.0

The remaining 146 stations (<= 2000 m a.s.l.) span elevations from -23.6 to 1985.0 m a.s.l. (range: 2008.6 m). The median elevation within this subset is 1193.5 m (25th to 75th percentile: 347.7 to 1550.1 m).

The stations under study in the research are shown in Figure 1.

3. Results and discussion

3-1. Regional clustering of synoptic stations and behavior of precipitation extremes

to delineate coherent hydro-climatic regimes across Iran, we applied K-means clustering (k = 5) to the 160-station network using standardized long-term seasonal means of Total Seasonal precipitation, R95p, R10mm, R20mm, Rx5day, and SPI across all four seasons. Standardization ensured equal weighting among intensity, frequency, and drought-related metrics. The resulting clusters (Figure 2) align strongly with major physiographic controls and large-scale circulation exposure rather than mere geographic proximity, suggesting that the partition captures dynamically meaningful precipitation regimes. Cluster 5 delineates the humid Caspian coastal belt and windward Alborz slopes, where seasonal totals exceed 250 mm in winter and approach 430 mm in autumn, accompanied by the largest R95p and Rx5day values. Cluster 1 occupies the north-central interior leeward of the Alborz and exhibits intermediate precipitation with a pronounced winter–autumn maximum. Cluster 2 corresponds primarily to the Zagros domain and adjacent western basins, characterized by moderate totals and heavy-rain frequencies shaped by orographic gradients. Cluster 3 encompasses the central and eastern plateau and south-eastern lowlands, displaying arid to semi-arid conditions with minimal exceedance frequencies and weak multi-day accumulations. Cluster 4 represents a single hyper-arid outlier station and is not considered a spatially coherent regime. A clear precipitation gradient emerges across clusters: Cluster 5 ≫ Cluster 1 > Cluster 2 > Cluster 3, with contrasts particularly amplified in autumn. These differences are consistently reflected in both mean totals and extreme indices (R95p and Rx5day), confirming that the K-means partition successfully isolates hydro-climatic regimes with sharply distinct extreme precipitation characteristics.

Figure 1. Synoptic stations used in this study.

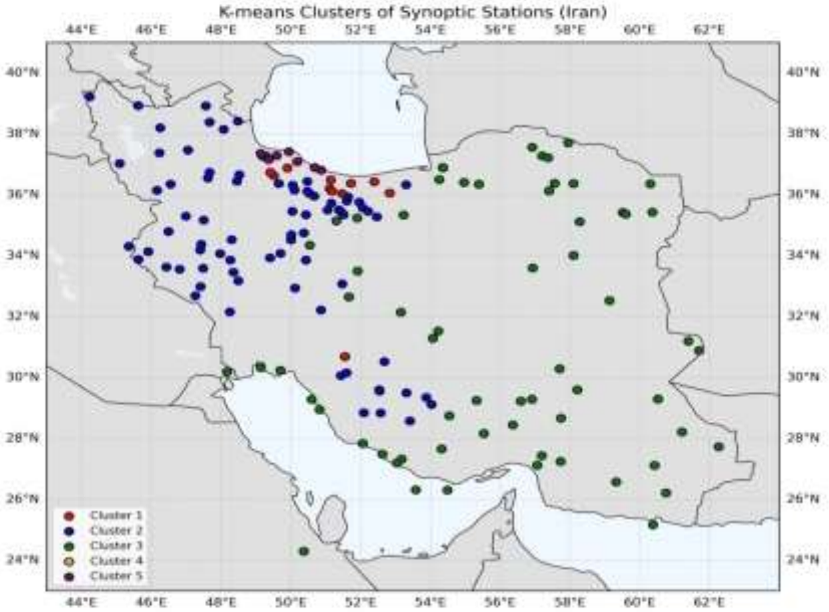

Figure 2. K-means clusters of synoptic stations (Iran).

3-2. Frequency of heavy precipitation events (R10mm and R20mm)

The temporal evolution of the frequency-based indices R10mm and R20mm for each cluster and season (Figure 3 a, b) highlights pronounced contrasts in both mean state and trends. Cluster 5 consistently exhibits the highest number of heavy-rain days in all seasons. In winter (DJF), the cluster-mean R10mm increases from roughly 4–5 days per season in the early 1980s to 10–12 days in recent decades, while R20mm grows from 2–3 to 5–8 days. A simple least-squares fit indicates an increase of approximately 1.1 R10mm days per decade and 0.6 R20mm days per decade in DJF. Autumn shows a similar though even more volatile behavior, with frequent seasons featuring more than 20 R10mm days and up to 16 R20mm days in the later part of the record. These trends suggest a substantial intensification of the frequency of heavy precipitation events in the Caspian–Alborz regime, consistent with increasing moisture availability and more efficient storm dynamics. Cluster 1 exhibits a qualitatively similar but somewhat weaker evolution. Winter R10mm counts rise from around 2–3 to 7–9 days per season, corresponding to an increase of about 1.2 days per decade, while R20mm increases by roughly 0.6 days per decade. Autumn again shows a marked upward shift in the late 1990s and 2000s, with more frequent seasons of 10–12 R10mm days. These changes point to a progressive enhancement of heavy-rain frequency over the north-central interior, albeit from a lower baseline than in the fully maritime Cluster 5.

By contrast, Clusters 2 and 3 show comparatively modest trends in R10mm and R20mm. In the western mountain cluster (Cluster 2), winter R10mm increases only slightly (≈0.2 days per decade), and the time series remains bounded between one and four days per season. The arid central–eastern cluster (Cluster 3) exhibits very low counts throughout, typically less than one R10mm day per season and virtually no R20mm exceedances, with only a marginal upward drift in winter. Summer (JJA) heavy-rain frequencies are negligible in all clusters except Cluster 5, where occasional convective seasons emerge after 2000, but without a clear monotonic trend. Together, these patterns indicate that the recent strengthening of heavy-rain frequency is largely confined to the Caspian–Alborz belt and, to a lesser extent, the north-central interior, while the western and eastern plateau regions remain dominated by infrequent but occasionally intense events.

3-3. Intensity and multi-day extremes (R95p and Rx5day)

The percentile-based index R95p and the maximum 5-day accumulation Rx5day provide complementary insight into changes in event intensity and multi-day storm behavior (Figures 3 c, d). In SON, R95p for Cluster 5 exhibits extreme interannual variability, with several seasons in the early 1980s and 2010s surpassing 400–600 mm. More importantly, there is a clear upward trend: a linear fit yields an increase of approximately 33 mm per decade, implying that the contribution of the wettest 5% of days to autumn rainfall has increased by more than a factor of two over the study period. Cluster 1 shows a very similar SON signal, with R95p increasing by about 35 mm per decade and episodic seasons exceeding 200 mm. Winter R95p also intensifies in both clusters, albeit with somewhat smaller slopes, underscoring a shift towards more extreme tail behavior in the wettest months.

In the western mountain cluster (Cluster 2), R95p displays moderate variability but only weak long-term change, while Cluster 3 remains characterized by low R95p values in all seasons. The absence of a pronounced trend in these interior regions suggests that the most dramatic intensification of event intensities is geographically constrained to the maritime north and north-west, where moisture fluxes from the Caspian Sea and the eastern Mediterranean are strongest. This is reinforced by the behavior of Rx5day. For Cluster 5, Rx5day in SON and DJF frequently exceeds 150–200 mm in recent decades, with several autumn seasons reaching beyond 200 mm, whereas early years in the record rarely surpass 100 mm. Cluster 1 shows an increase from typical values of 30–40 mm to 80–110 mm in recent decades. By contrast, Rx5day in Clusters 2 and 3 remains mostly below 70 mm and 40 mm, respectively, with only modest trends. These results imply that the potential for prolonged multi-day storm episodes has increased substantially in the Caspian–Alborz and north-central regimes, heightening the risk of large-scale flooding and landslides in these densely populated and topographically complex areas.

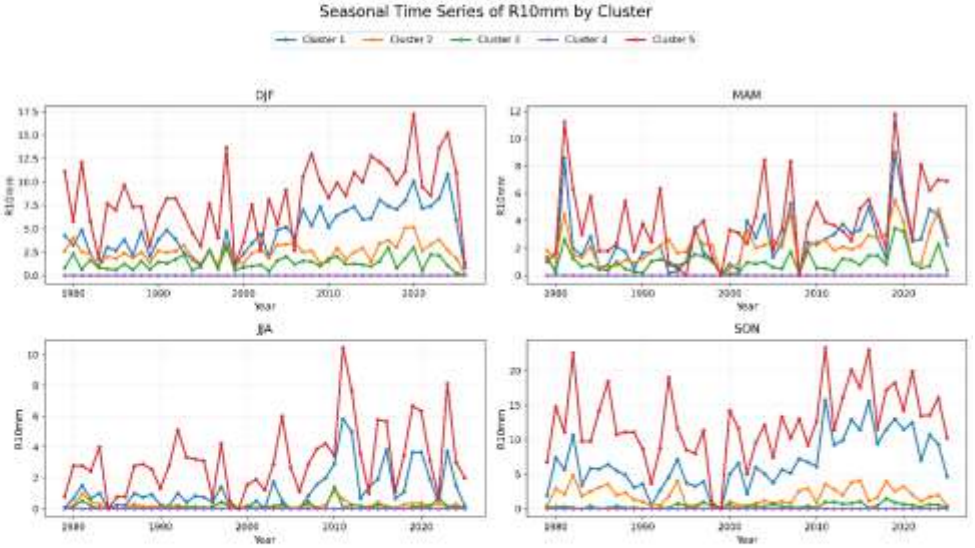

(a)

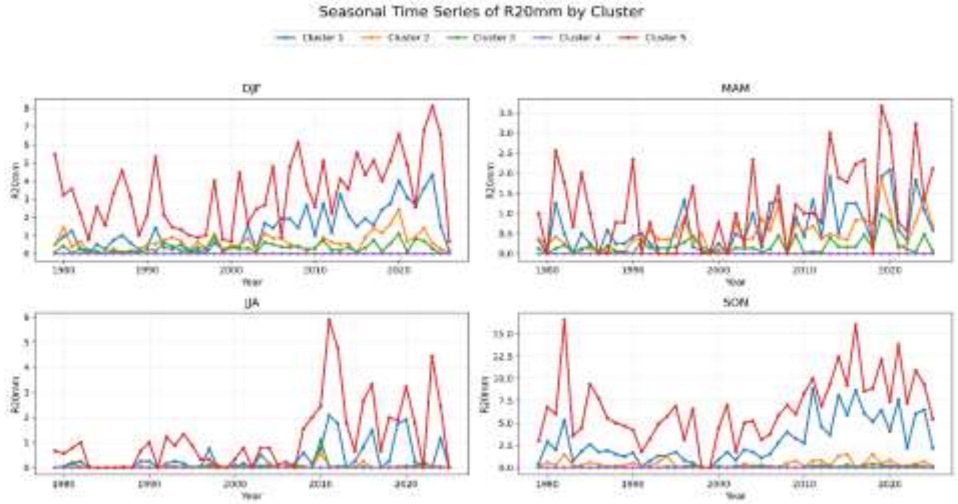

(b)

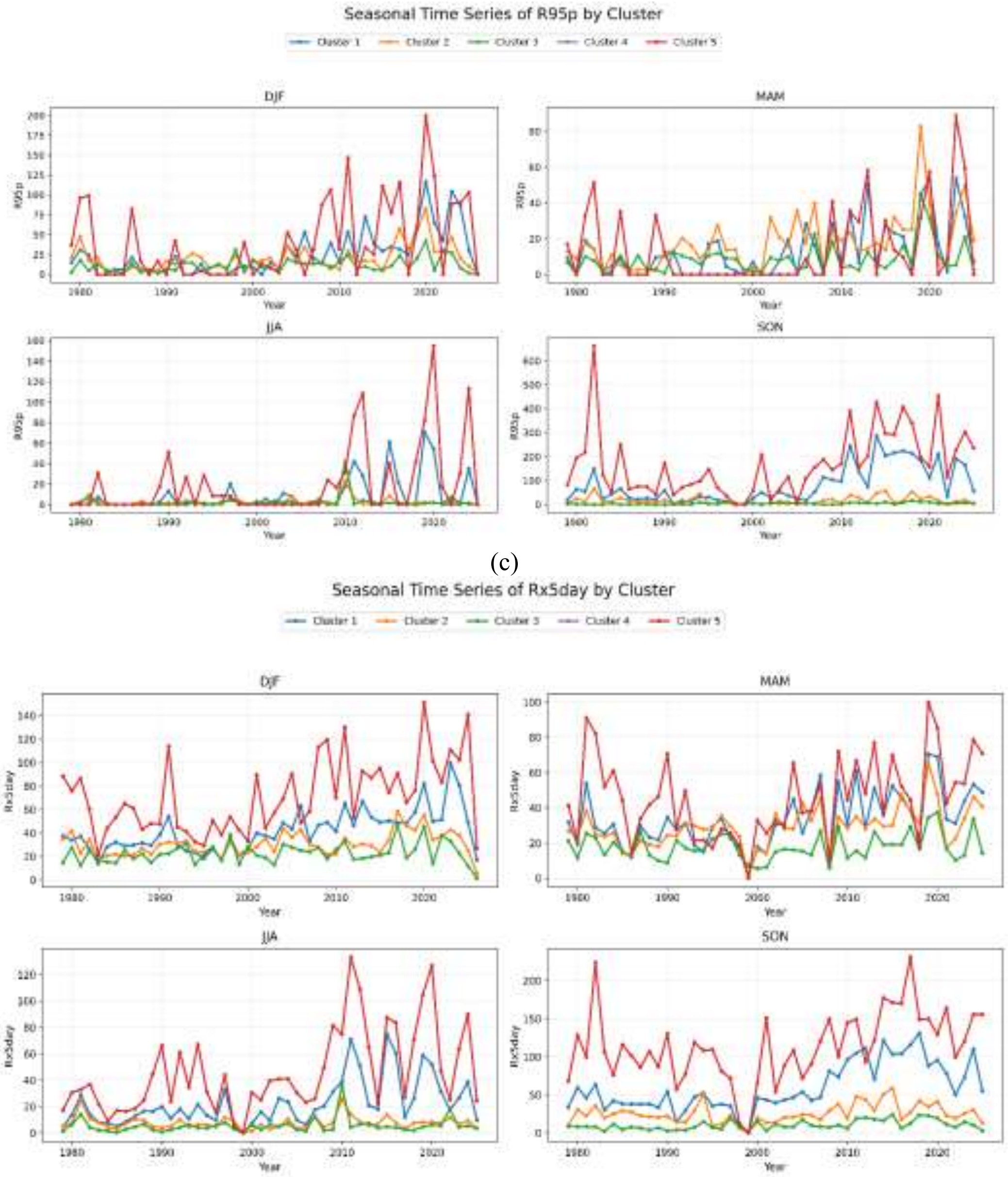

(c)

(d)

Figure 3. Seasonal time series of R10mm (number of days with precipitation ≥10 mm) for each cluster and season (a), R20mm (days with precipitation ≥20 mm (b), Seasonal time series of R95p (precipitation total on days above the 95th percentile) for each cluster and season (c), Seasonal time series of Rx5day (maximum 5-day precipitation) for each cluster and season (d).

3-4. Drought variability and seasonal totals (SPI and Total Seasonal)

The cluster-wise Standardized Precipitation Index (SPI) time series (Figure 4, a) reveal that all regions share a number of basin-wide drought episodes, most notably the severe multi-year drought around 1998–2001, which is evident in all seasons and clusters as SPI values below −3. Subsequent decades are characterized by a partial recovery and enhanced wetness in winter, particularly in Clusters 1 and 5, where DJF SPI trends are approximately +0.3 and +0.2 per decade, respectively. Nevertheless, the most recent years of the record again show sharp negative excursions, hinting at a possible re-emergence of sustained dryness under continuing climate variability and change. The central–eastern plateau (Cluster 3) displays a slight negative trend in DJF SPI, consistent with its marginal increase in heavy-rain metrics but persistently low seasonal totals. Seasonal accumulation, expressed by the Total Seasonal index (Figure 4, b), integrates these patterns into a regionally distinct picture of changing wetness. In winter, Cluster 5 shows an increase from about 200–250 mm per season in the early record to 350–500 mm in recent decades, corresponding to a trend of roughly 33 mm per decade. Cluster 1 follows a comparable trajectory with a trend of about 31 mm per decade, while Clusters 2 and 3 display only weak or negligible changes. The most dramatic shifts, however, occur in autumn. SON totals for Cluster 5 rise from 200–300 mm to 500–800 mm, with a linear trend near 49 mm per decade; Cluster 1 again shows a strong positive trend (~53 mm per decade). In contrast, the western mountain and eastern plateau clusters exhibit little long-term change in SON totals. Summer and spring totals remain low in all regions except the Caspian belt, where JJA rainfall displays sporadic but substantial increases associated with convective outbreaks and monsoon-like intrusions from the south.

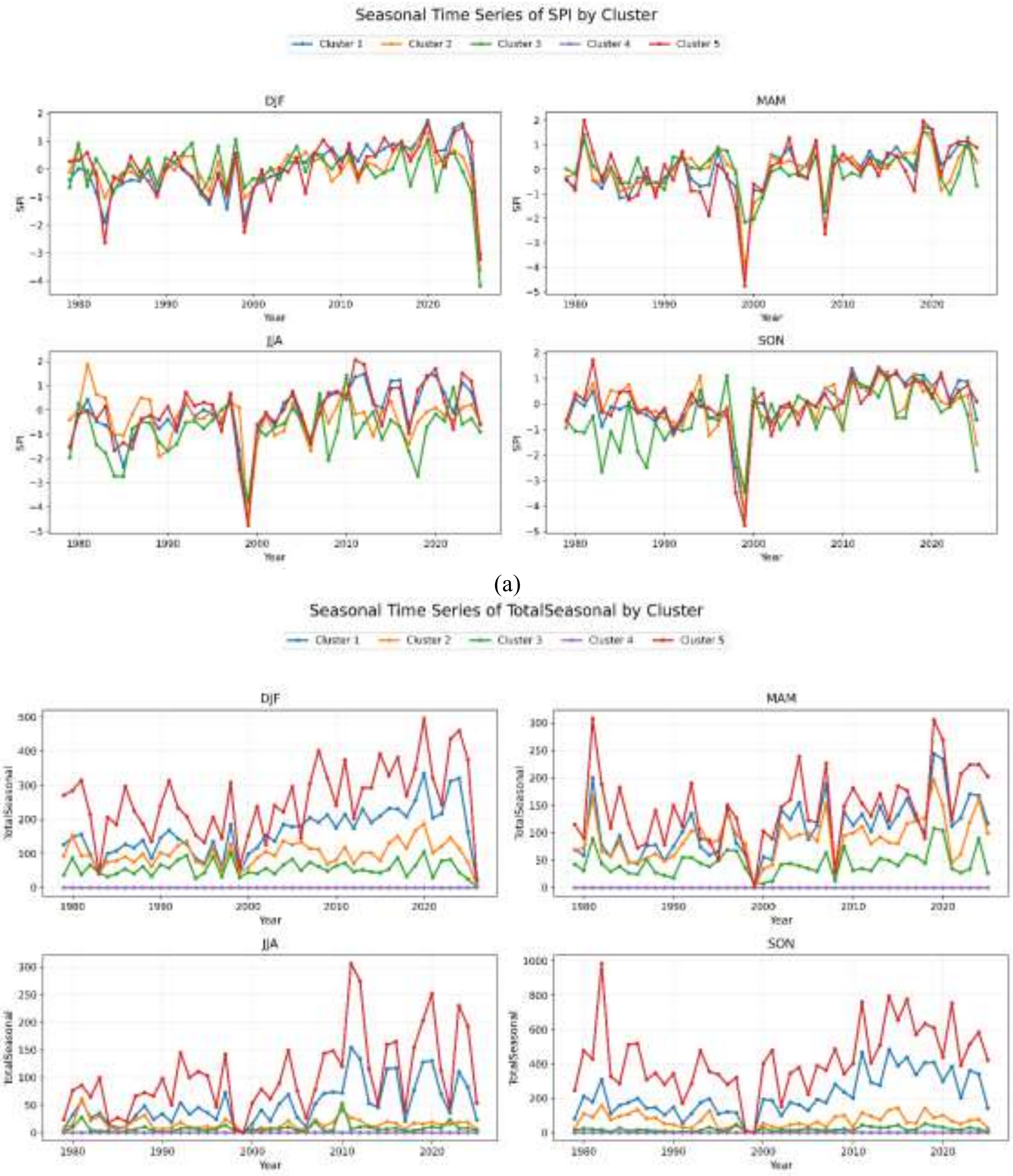

(a)

(b)

Figure 4. Seasonal time series of SPI for each cluster and season (a), Seasonal time series of Total Seasonal precipitation for each cluster and season (b).

3-5. Network-Metric Diagnostics of Teleconnection Influence (1979–2024; Directed & Weighted Climate Network)

In this study, “causal strength” refers to the absolute magnitude of the edge weights estimated by PCMCI+, derived from partial correlation (Par Corr) or normalized conditional mutual information. These weights quantify conditional statistical dependence after controlling for autocorrelation and confounding variables, and therefore represent directed statistical influence rather than deterministic physical causation. We emphasize that the inferred network encodes statistical causal influence estimated by PCMCI+ rather than deterministic physical control. In this framework, node degree captures how many teleconnections directly condition the target extreme-precipitation node, node strength reflects the cumulative magnitude of causal influence (absolute edge weights from partial correlation/conditional mutual information), and betweenness centrality highlights indices that mediate multi-step pathways. Across regions, Atlantic-sector indices emerge as the most influential drivers, consistent with their role in modulating the Mediterranean storm track and the downstream Rossby wave-train over West Asia. In practical terms, enhanced Atlantic variability is linked to systematic shifts in jet latitude and the positioning of upper-level troughs over the Mediterranean–Turkey corridor, which jointly govern moisture transport into western and northern Iran. Indices with high betweenness (e.g., EAWR/NAO in specific seasons) are therefore interpreted as circulation ‘gatekeepers’ that translate upstream Atlantic anomalies into regional jet-stream reconfiguration and storm track deflection.

The 1980–1999 versus 2000–2024 comparison indicates that the strongest links persist, while weaker connections show greater sampling uncertainty due to shorter sub-period lengths. We therefore interpret secondary links cautiously and focus on robust edges that remain stable across sensitivity checks (FDR control and alternative lag windows).

Node set: Two node categories are analyzed: (i) teleconnection indices (AMO, DMI, EAWR, MEI, NAO, NINO3.4, ONI, SOI, TNA, TSA, WP, AO), and (ii) precipitation-related indices labeled by cluster (e.g., R10mm_C1, Rx5day_C3, SPI_C5, TotalSeasonal_C2). The full network contains 36 nodes; the teleconnection-only subset contains 12 nodes. (Figure 5 a, b, c, d).

Directed connectivity: In-degree/out-degree quantify the number of incoming/outgoing links, while total degree is their sum. In-strength/out-strength quantify the sum of incoming/outgoing edge weights. Because weights can be signed, strengths may be negative, indicating dominance of negative associations for the corresponding incoming/outgoing link set. Net-strength is defined here as out-strength minus in-strength; positive values suggest a more 'exporting' node in the signed-weight sense (Table 3). The term “dominance” is used here strictly in a statistical-network sense, referring to higher connectivity and mediation capacity, rather than implying deterministic physical control over regional precipitation. Betweenness centrality: Betweenness reflects the fraction of shortest paths traversing a node and is commonly interpreted as a measure of mediation or brokerage between otherwise weakly connected node groups. In climate-network applications, high-betweenness nodes often align with dynamically important modes that couple remote regions or regimes (Figure d).

Across the full network, teleconnection nodes exhibit markedly higher connectivity and brokerage than precipitation-index nodes, consistent with the role of large-scale modes as network backbones that link multiple regional indicators. Precipitation nodes show smaller degrees and near-zero betweenness for most indices, implying that they behave primarily as recipients or local endpoints rather than global mediators.

Table 3. Mean ± SD of key metrics by node type (signed strengths).

Node type	N	total degree	indegree	outdegree	in strength	out strength	betweenness	net strength
teleconnection	12	19.333 ± 10.228	9.833 ± 5.042	9.500 ± 5.231	1.055 ± 2.535	1.053 ± 2.308	0.069 ± 0.080	-0.002 ± 0.643
precip	24	15.250 ± 4.910	7.542 ± 2.536	7.708 ± 2.386	3.839 ± 1.033	3.840 ± 1.482	0.026 ± 0.039	0.001 ± 1.361

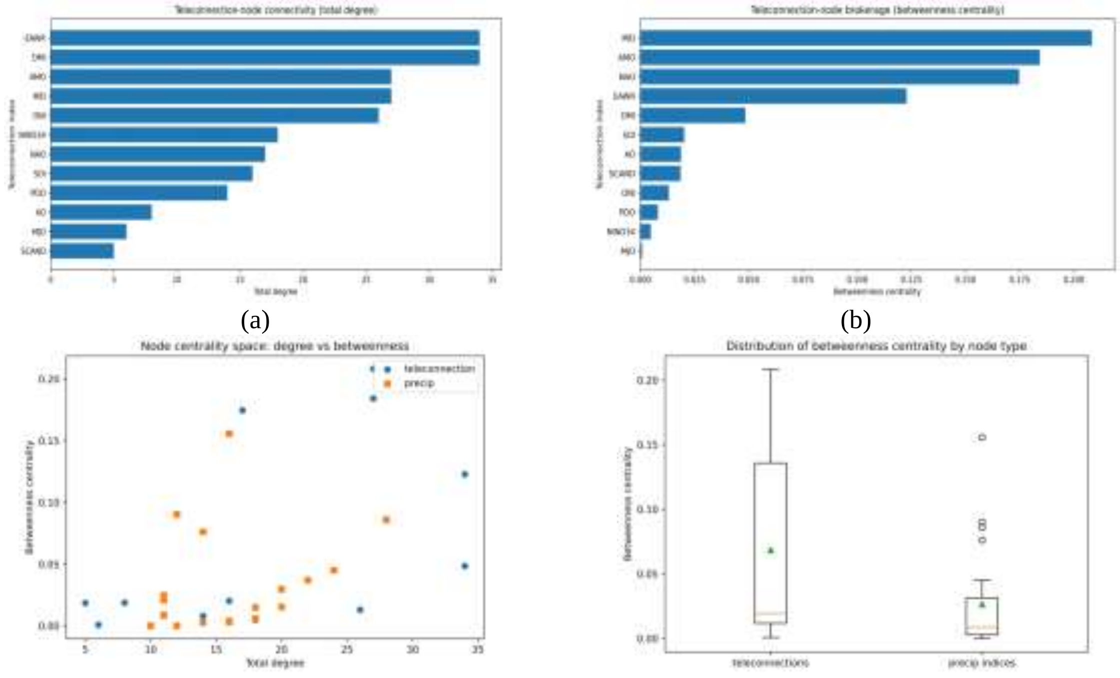

(a) (b)

(c) (d)

Figure 5. Total degree of teleconnection nodes (teleconnection-only file), sorted. Larger values indicate broader connectivity (a), Betweenness centrality of teleconnection nodes (teleconnection-only file), sorted. Larger values indicate stronger brokerage roles (b), Degree–betweenness 'centrality space' for all nodes. Teleconnections cluster toward higher degree and betweenness compared with precipitation indices (c), Distribution of betweenness centrality by node type (boxplot with means) (d).

Table 4. Top 10 nodes by betweenness centrality (full network).

Node	Type	betweenness	total degree	indegree	outdegree	community	net strength
MEI	teleconnection	0.2083	27	13	14	1	-1.729
AMO	teleconnection	0.1842	27	14	13	0	0.353
NAO	teleconnection	0.1747	17	10	7	5	-0.495
SPI_C5	precip	0.1557	16	8	8	4	-1.243
EAWR	teleconnection	0.1228	34	17	17	1	-0.067
TotalSeasonal_C1	precip	0.0903	12	6	6	3	0.000
TotalSeasonal_C2	precip	0.0859	28	14	14	2	0.000
SPI_C1	precip	0.0761	14	7	7	3	-0.483
DMI	teleconnection	0.0484	34	17	17	1	0.000
R20mm_C2	precip	0.0451	24	12	12	2	0.000

The highest-betweenness nodes are predominantly teleconnection indices, underscoring their role as bridges connecting multiple precipitation indicators across clusters. In this dataset, the strongest brokerage signal is associated with MEI, followed by AMO and NAO, with DMI and EAWR also displaying comparatively large betweenness values. Such nodes are natural candidates for physical interpretation, predictor screening, and sensitivity experiments (Table 5).

Table 5. Teleconnection-node metrics (teleconnection-only network), sorted by betweenness.

Node	total degree	Betweenness	indegree	outdegree	in strength	out strength	net strength	community
MEI	27	0.2083	13	14	3.499	1.770	-1.729	1
AMO	27	0.1842	14	13	-3.442	-3.088	0.353	0
NAO	17	0.1747	10	7	1.800	1.305	-0.495	5
EAWR	34	0.1228	17	17	3.174	3.107	-0.067	1
DMI	34	0.0484	17	17	4.115	4.115	0.000	1
SOI	16	0.0203	8	8	-3.044	-2.286	0.758	1
AO	8	0.0187	4	4	0.088	0.088	0.000	5
SCAND	5	0.0185	3	2	-1.010	-0.723	0.287	5
ONI	26	0.0131	13	13	3.284	4.008	0.724	1
PDO	14	0.0080	7	7	0.900	0.990	0.090	1
NINO3.4	18	0.0047	9	9	2.741	2.794	0.052	1
MJO	6	0.0008	3	3	0.552	0.552	0.000	0

Table 6. Top 10 precipitation-index nodes by total degree (full network).

Node	total degree	betweenness	community	indegree	outdegree
TotalSeasonal_C2	28	0.0859	2	14	14
R20mm_C2	24	0.0451	2	12	12
SPI_C3	22	0.0370	0	11	11
TotalSeasonal_C3	20	0.0296	0	10	10
Rx5day_C2	20	0.0153	2	10	10
Rx5day_C3	18	0.0150	0	9	9
R95p_C2	18	0.0057	2	9	9
SPI_C5	16	0.1557	4	8	8
R10mm_C2	16	0.0039	2	8	8
SPI_C2	16	0.0030	2	8	8

Among precipitation metrics, Total Seasonal_C2 and R20mm_C2 emerge as the most connected response nodes, with SPI_C3 and Rx5day_C5 also exhibiting elevated degree and strength (Table 6). This hierarchy is physically meaningful rather than purely topological. Cluster C2 largely corresponds to the western–orographic regime influenced by Mediterranean cyclogenesis and Zagros uplift, where both seasonal accumulation and heavy-rain thresholds respond sensitively to upstream jet positioning and moisture transport corridors. The co-activation of threshold-based (R20mm) and accumulation-based (Total Seasonal) indices suggests that teleconnection forcing does not merely modulate isolated extreme days, but reorganizes the synoptic environment in a way that alters both event frequency and seasonal water budgets. The network diagnostics reveal a marked structural asymmetry: large-scale teleconnection modes occupy central positions (high degree and betweenness), whereas cluster-level precipitation indices are comparatively peripheral. This configuration is dynamically consistent with the direction of information flow in the climate system. Teleconnections such as ENSO, AMO, and EAWR represent basin-scale reorganizations of SST gradients and planetary-wave structure that project onto the Mediterranean–West Asia waveguide, thereby shifting jet-stream latitude, baroclinic growth zones, and moisture convergence axes. In contrast, precipitation indices are local expressions of these upstream circulation adjustments. High-betweenness nodes—particularly MEI and AMO in the present network—function as statistical “gatekeepers.” Dynamically, this suggests that tropical Pacific variability (ENSO family) and multidecadal Atlantic background states modulate the phase alignment of Rossby wave trains entering Eurasia. When these modes are in conducive phases, the subtropical jet entrance region tends to align with the eastern Mediterranean–Iran corridor, enhancing upper-level divergence and synoptic ascent; in opposing phases, the jet core is displaced poleward or equatorward, suppressing organized precipitation. Thus, the identified gatekeeper role is consistent with a wave-dynamical control mechanism rather than a purely statistical artifact. Signed strengths require cautious interpretation. Negative in- or out-strength values indicate that inverse relationships dominate incident links (e.g., drought-favoring phases), not diminished influence. Therefore, absolute strength provides a better measure of overall leverage, whereas the sign encodes the physical direction of response (wet-favoring vs dry-favoring regimes). For mechanistic clarity, both signed and absolute summaries are reported. From an applied perspective, the network structure implies that monitoring a limited subset of dynamically efficient teleconnections (notably ENSO-family indices and AMO) may provide early indication of cluster-specific extreme-precipitation risk, particularly in western and southern Iran where multi-index coherence is strongest. The findings therefore move beyond correlation by linking statistical centrality to physically interpretable circulation pathways and regionally differentiated hydroclimatic responses (Hersbach et al., 2020; Haas et al., 2023; Saha, & Gupte, 2023; Odenweller & Donner, 2020; Kohler et al., 2021; Shang et al., 2022; Fan et al., 2022; Mathbout et al., 2020; Liu et al., 2023; Traag et al., 2019; Meshcheryakova, & Shvydun, 2024; Kuai et al., 2023).

3-5-1. Limitations and Recommended Extensions

Because the spreadsheets contain node metrics but not the underlying edge list, interpretation is constrained to topological summaries. For a complete manuscript workflow, we recommend (i) providing the adjacency matrix or edge list (including sign and weight), (ii) repeating the analysis across sensitivity settings (threshold choice, lag structure, season definition), and (iii) quantifying robustness via bootstrap resampling of years or events. If causal discovery is an objective, coupling these metrics with Bayesian-network or graphical-model methods provides a defensible pathway from association networks to directed dependence hypotheses**.** In order to better analyze the results and effects of teleconnections index on the stations in the southern half of the country, its changes are as follows:

3-5-2. New Analysis for Southern Region

Inputs consist of (i) seasonally aggregated precipitation-extreme indices for southern Iran derived from IRIMO observations (Islamic Republic of Iran Meteorological Organization; 1979–2024), and (ii) PCMCI output matrices encoding directed teleconnection → precipitation links, their lag structure (0–1 season), and standardized effect sizes. The precipitation metrics include PRCPTOT (seasonal total precipitation), R10mm and R20mm (counts of days exceeding 10 and 20 mm), Rx1day (maximum 1-day precipitation), Rx5day (maximum 5-day precipitation), and the moderate-threshold index R5mm (as represented in the PCMCI outputs).

Teleconnection predictors comprise ENSO diagnostics (Niño-3.4 SST anomalies, ONI, MEI, and SOI), the Dipole Mode Index (DMI; IOD), EAWR (East Atlantic/Western Russia pattern), the Atlantic Multidecadal Oscillation (AMO), and the Arctic Oscillation (AO). All indices entering the PCMCI framework are standardized (suffix "_std"), ensuring comparability of estimated link magnitudes across precipitation targets. PCMCI—a two-stage procedure combining PC-based condition selection with momentary conditional independence (MCI) testing—is employed to infer directed dependencies in high-dimensional, autocorrelated time series while minimizing spurious associations induced by common drivers. Retained links are interpreted as conditional statistical evidence of directional influence consistent with temporal ordering; nevertheless, residual confounding, finite-sample effects, and potential model misspecification cannot be fully excluded and are discussed in the limitations section. A synthesis of teleconnection influence patterns is provided in Table 7.

Figure 6 visualizes the same ranking. The conspicuous dominance of ENSO-family indices is not merely a numerical accident: it reflects a coherent dynamical "teleconnection backbone" by which tropical Pacific variability can modulate moisture transport, upper-level divergence, and synoptic storm-track positioning over West Asia.

Aggregating across seasons, the cumulative teleconnection signal is largest for Rx1day and Rx5day, implying that the most intense short-duration events are particularly susceptible to large-scale circulation reconditioning. In contrast, moderate wet-day counts (e.g., R10mm) show a more diffuse and weaker dependency structure (Table 8).

The causal connectivity is strikingly seasonal. SON contains the largest portion of the teleconnection signal, consistent with the climatological transition season when subtropical jets, moisture pathways from the Arabian Sea/Persian Gulf, and remote forcing from the Indian and Pacific oceans can align to amplify rainfall variability. MAM also shows strong coupling, whereas DJF is more selectively controlled—especially by EAWR—and JJA is nearly link-free in the retained network. The results are shown in Figure 7.

Table 7. Overall influence ranking (all indices × seasons).

Teleconnection	Total aggregated |strength|	Share of total (%)
NINO3.4	5.13	17.8
ONI	4.78	16.6
MEI	4.37	15.2
SOI	4.23	14.7
DMI	3.78	13.1
EAWR	2.98	10.4
AMO	2.88	10.0
AO	0.63	2.2

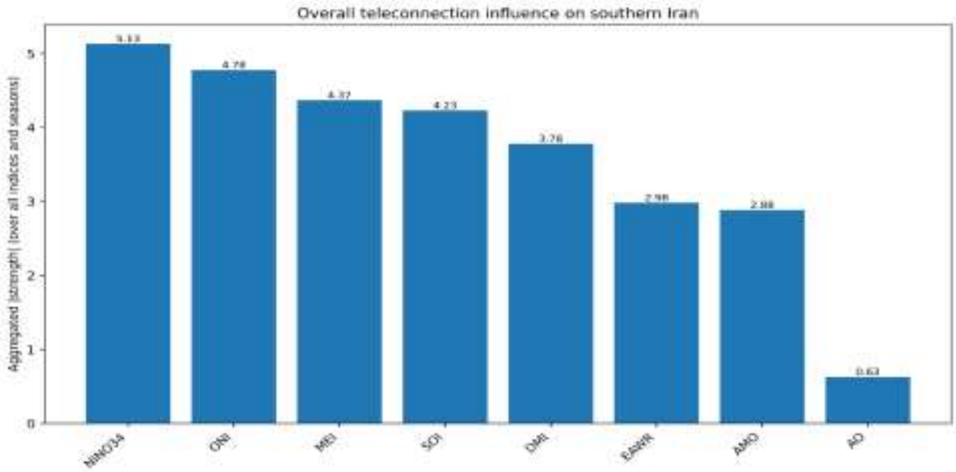

Figure 6. Overall teleconnection influence on southern Iran (sum of absolute PCMCI strengths over indices and seasons).

Table 8. A compact quantitative decomposition is provided below (column sums over all teleconnections)

Precipitation index	Total |strength|	Share of total (%)
Rx1day_std	6.03	21.0
PRCPTOT_std	5.36	18.6
R10mm_std	5.25	18.2
R5mm_std	4.72	16.4
R20mm_std	3.80	13.2
Rx5day_std	3.63	12.6

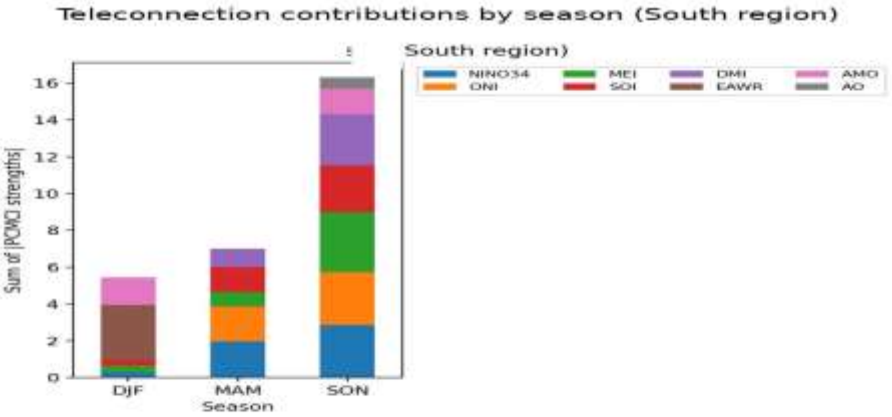

Figure 7. Teleconnection contributions partitioned by season. Note the winter dominance of EAWR and the autumn prominence of DMI alongside ENSO indices.

Most retained links occur at lag 0 (teleconnection and precipitation index within the same season), while a smaller subset appears at lag 1. The retained edge count by lag is lag 0 = 61 and lag 1 = 8 (total = 69). The dominance of contemporaneous links suggests that precipitation extremes over southern Iran respond primarily to the instantaneous large-scale circulation configuration rather than to long memory processes. However, the presence of lag-1 connections—particularly AMO → DJF—indicates a modest preconditioning pathway, consistent with multidecadal Atlantic SST variability influencing hemispheric circulation states that persist into the subsequent winter. Occasional AO and MEI lag-1 links in SON/MAM further imply that autumn and spring transitions may carry memory through stratosphere–troposphere coupling (AO) or delayed ENSO teleconnection adjustment. Because the aggregated matrices use absolute strengths, they quantify the magnitude of teleconnection leverage rather than its polarity. The signed edge list clarifies that both wet-favoring and dry-favoring pathways coexist. In particular, SOI links are frequently negative, which is dynamically consistent: SOI is anti-correlated with Niño3.4/ONI, so its sign reversal reflects the canonical ENSO phase dependence rather than contradictory behavior. Although PCMCI is statistical in construction, the inferred hierarchy aligns with well-established dynamical pathways. ENSO-family dominance across multiple precipitation targets—especially Rx1day and Rx5day—is physically interpretable. Tropical Pacific SST anomalies reshape the Walker circulation, alter diabatic heating gradients, and project onto Eurasian Rossby wave trains. These wave trains modulate the latitude and intensity of the subtropical jet and the position of upper-level divergence maxima over the eastern Mediterranean–Iran corridor. When the jet entrance/exit region aligns with the target domain, synoptic ascent and baroclinic growth are enhanced, increasing the probability of short-duration extreme events. This explains why intensity-based metrics (Rx1day/Rx5day) show greater network connectivity than moderate wet-day frequency indices: extreme events are more sensitive to dynamical lift plus moisture convergence than to background drizzle conditions. The IOD (DMI) acts as a secondary but physically coherent driver by reorganizing Indian Ocean convection and modifying moisture transport from the Arabian Sea into southern Iran. Its signal is strongest when tropical Indian Ocean heating anomalies reinforce ENSO-induced wave trains, highlighting constructive interference between basins. EAWR's winter prominence (DJF) is dynamically plausible. The EAWR pattern reorganizes the Euro-Atlantic waveguide and longitudinal placement of ridge–trough systems, thereby steering Mediterranean cyclogenesis and storm-track incursions into West Asia. Its seasonal specificity reflects the greater efficiency of Rossby-wave propagation during winter when the jet is strongest. AMO's weaker but detectable signal, including lag-1 edges, is consistent with slow Atlantic boundary forcing. Multidecadal SST anomalies modulate the background meridional temperature gradient and hence the preferred stationary-wave configuration. The identified lag-1 links likely represent circulation preconditioning rather than rapid forcing. Across southern Iran, teleconnection influence is neither spatially uniform nor seasonally stationary. The strongest network signal is concentrated in SON and MAM, dominated by ENSO-related indices, with IOD (DMI) as the principal secondary contributor and EAWR as a winter-specialist mode. The concentration of strong edges in short-duration extreme metrics implies that seasonal-to-interannual predictability may be higher for extreme-event propensity than for moderate rainfall frequency—provided that tropical SST states are forecast with skill.

Taken together, the network does not merely show statistical association; it delineates a physically consistent hierarchy in which basin-scale SST anomalies reorganize jet-stream geometry, wave-train phase, and moisture pathways, thereby modulating the dynamical environment required for extreme precipitation over Iran (Abid et al., 2020; Gong et al., 2024; Dehghani et al., 2020; Ehsan et al., 2020; Esmaeilpour et al., 2021; Krich et al., 2020; Zarrin et al., 2022; Zhang et al., 2022). In the subsequent phase of this research, we will examine composite patterns across multiple atmospheric levels to diagnose how the teleconnection modes most relevant to extreme precipitation manifest throughout the troposphere and the stratosphere. Notwithstanding the breadth of the resulting fields, only a carefully curated subset of the most robust and physically interpretable signals is presented and discussed herein, thereby ensuring that neither the narrative coherence nor the mechanistic clarity is compromised.

3-6. The analysis of 250 (hPa) Level

3-6-1. Overview

The supplied composites depict 250-hPa wind-speed anomalies (shading) alongside horizontal wind-vector anomalies (arrows) for seasons AMJ, JFM, and OND over 1979–2024. The panels are conditioned on specific teleconnection indices and phases (e.g., AMO, EAWR, and ENSO-family metrics such as Niño-3.4, ONI, MEI, and SOI). Local stippling marks grid points where anomalies reach statistical significance at $p<0.05$, whereas the headline r and p values summarize a domain-mean correlation between the wind-speed anomaly field and the index anomaly. Notwithstanding the attractive spatial coherence of several panels, some composites are based on small event counts (N≈4–7); therefore, the interpretation below emphasizes robust spatial motifs, consistency across related indices, and physically plausible jet-stream adjustments rather than a single deterministic narrative.

3-6-2. Cross-panel synthesis: what is common and what is distinct

Across seasons, the composites repeatedly organize into a meridional dipole in jet strength—i.e., enhanced westerlies in one latitude band accompanied by weakened flow elsewhere—which is consistent with a latitudinal displacement and/or longitudinal re-phasing of the Eurasian jet (Manney et al., 2021). In the ENSO-related panels, the most salient feature is a coherent jet streak extending from North Africa toward the Middle East, whereas in the EAWR panels the dominant signal resembles a wave train-like see-saw between the Euro-Atlantic sector and western Russia (Lemus-Canovas, 2022; Halifa-Marín et al., 2025). Importantly, the maps suggest that DJF-season extremes are preferentially accompanied by either an intensified subtropical jet over the eastern Mediterranean–Iran corridor or, conversely, a weakened mid-latitude jet over the same corridor; these two regimes are not mutually exclusive in principle, yet neither can they be invoked indiscriminately without reference to the governing index phase (Jiménez-Esteve and Domeisen, 2020). In Table 9 presents Panel metadata (the maps in Figure 8 a-j). More explicitly, EAWR-negative phases in JFM correspond to a southward-displaced Euro–Atlantic jet core and enhanced downstream troughing over the eastern Mediterranean, thereby increasing upper-level divergence and baroclinic development over western Iran. Conversely, ENSO-positive phases project onto a strengthened subtropical jet branch extending from North Africa toward Southwest Asia, modifying Rossby-wave propagation pathways and favoring synoptic-scale ascent. These phase-dependent jet adjustments provide the dynamical bridge linking remote SST anomalies to regional precipitation extremes.

3-6-3. Detailed interpretation (panel-by-panel)

Figure 8 summarizes upper-tropospheric wind-speed composites linked to key teleconnection phases. Interpretations are weighted by the domain-mean correlation strength and its statistical support, to avoid over-generalization from marginal composites.

In AMJ, ENSO-related phases show spatially coherent but statistically constrained jet rearrangements. Under Niño-3.4 negative conditions **(**Figure 8a**),** wind-speed anomalies indicate enhanced high-latitude flow over northern Eurasia, accompanied by weakened westerlies from the central-to-eastern Mediterranean into West Asia, consistent with a poleward-shifted jet core. The ONI positive composite **(**Figure 8b**)** similarly reflects a redistribution of jet momentum across southeastern Europe toward the Black Sea–Caucasus sector. Although domain-mean correlations remain weak-to-marginal ($p \gtrsim 0.08$–0.10), the spatial coherence suggests structured circulation adjustments rather than purely random noise; therefore, these AMJ panels are treated as dynamical context rather than primary evidence.

Table 9. Panel metadata (season, index, phase, n, r, p).

Panel	Season	Index	Phase	n	r	p
A	AMJ	AMO	NEG	7	0.014	0.942
B	AMJ	NINO3.4	NEG	4	0.320	0.079
C	AMJ	ONI	POS	4	0.306	0.094
D	JFM	AMO	NEG	7	-0.297	0.105
E	JFM	EAWR	NEG	5	0.518	0.002
F	JFM	EAWR	POS	6	0.518	0.002
G	JFM	MEI	POS	4	0.454	0.010
H	JFM	NINO3.4	NEG	4	0.459	0.009
I	JFM	SOI	NEG	4	-0.472	0.007
J	OND	EAWR	POS	5	0.660	$p \approx 5\times10^{-5}$

In JFM, the signal becomes robust. The EAWRnegative and EAWRpositive composites **(**Figure 8c–d**)** exhibit a clear, phase-symmetric modulation of the Euro-Atlantic jet, with domain-mean correlations that are statistically significant (r ≈ 0.52, p ≈ 0.002–0.003). This symmetry supports the interpretation of EAWR as an efficient dynamical “switch” that steers jet latitude and downstream wave-guiding toward the Mediterranean–West Asia sector. ENSO-family diagnostics in JFM (MEI positive, Niño-3.4 negative, SOInegative; Figure 8 e–g**)** consistently strengthen the subtropical jet from North Africa toward the eastern Mediterranean and Iran (r ≈ 0.45–0.47, p < 0.01). The agreement across multiple ENSO indices provides robustness against index-specific artifacts, even under limited extreme-event sample size.

InOND**,** EAWR positive **(**Figure 8h**)** yields the strongest association in the figure set (r ≈ 0.66, p ≈ 5×10^{-5}), characterized by a pronounced mid-latitude enhancement band across Europe into western Russia and compensating weakening over the Mediterranean/North Africa sector. This configuration implies a shifted storm-track latitude and altered downstream jet-exit dynamics, highlighting EAWR as the dominant circulation lever for OND extremes within the composite framework.

Overall, the strongest and most interpretable jet modulation is concentrated in EAWR (JFM and OND) and ENSO-family indices (JFM)**,** whereas AMJ composites are retained primarily for contextual consistency (Glantz & Ramirez, 2020; L’Heureux et al., 2024; Luo et al., 2023; Marshall, 2021; Toreti et al., 2010; Vacca et al., 2025; Webb & Magi, 2022; Zhang et al., 2019).

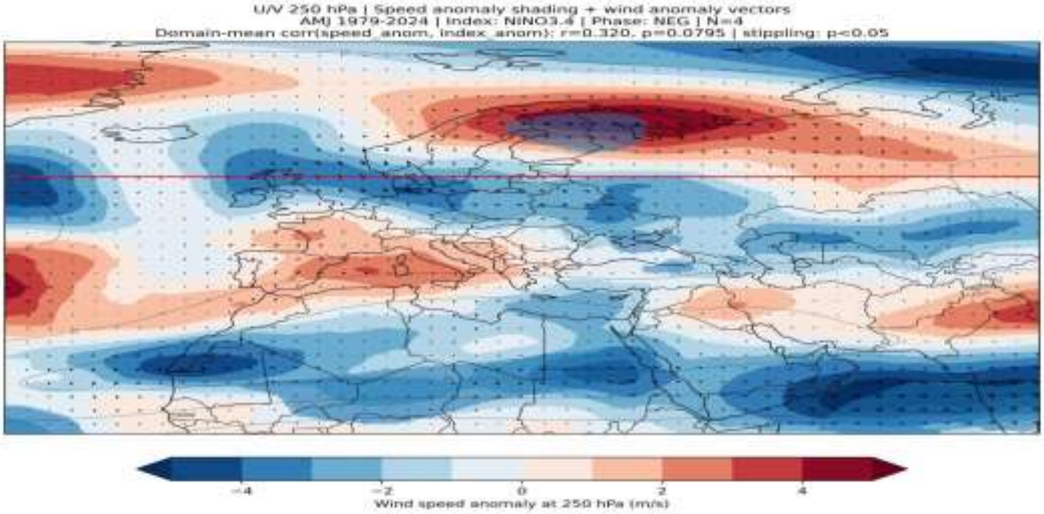

(a)

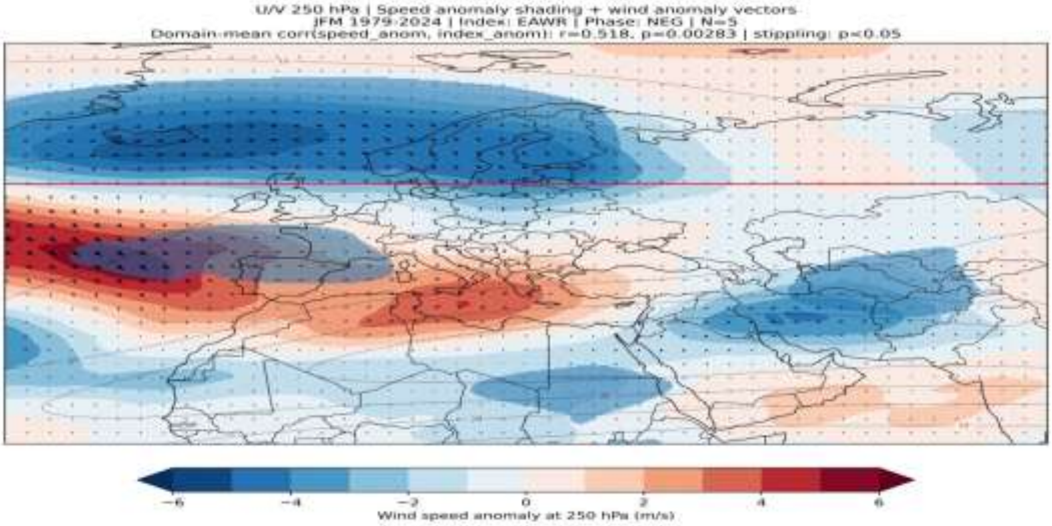

(b)

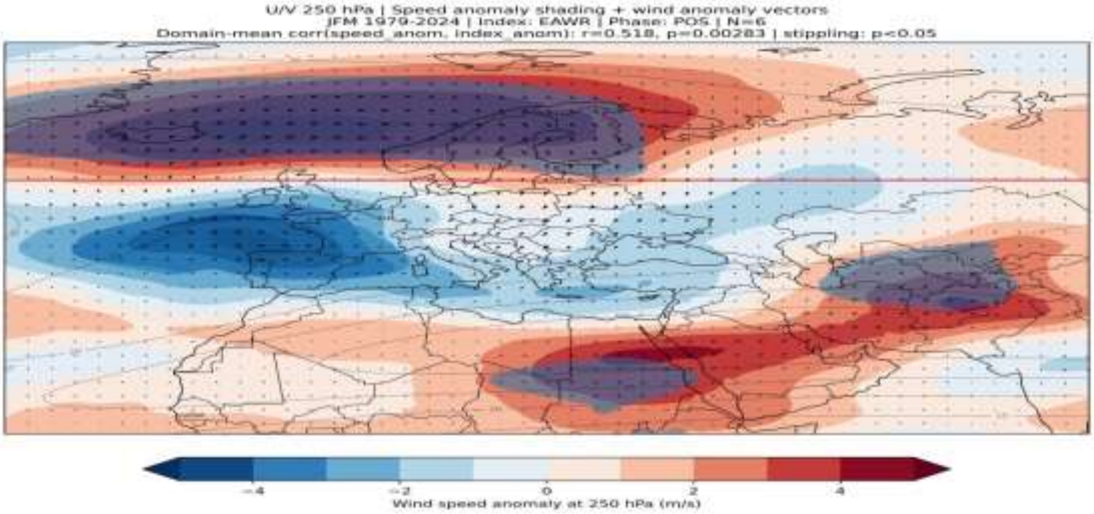
U/V 250 hPa | Speed anomaly shading + wind anomaly vectors
JFM 1979-2024 | Index: EAWR | Phase: POS | N=6
Domain-mean corr(speed_anom, index_anom): r=0.518, p=0.00283 | stippling: p<0.05
−4
−2
0
2
4
Wind speed anomaly at 250 hPa (m/s)

(c)

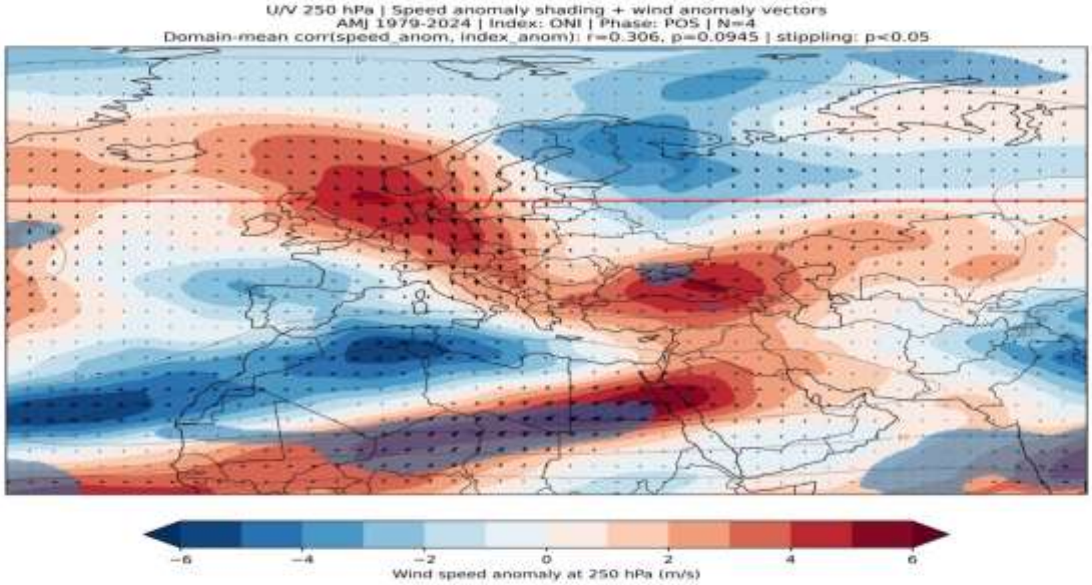
U/V 250 hPa | Speed anomaly shading + wind anomaly vectors
AMJ 1979-2024 | Index: ONI | Phase: POS | N=4
Domain-mean corr(speed_anom, index_anom): r=0.306, p=0.0945 | stippling: p<0.05
−6
−4
−2
0
2
4
6
Wind speed anomaly at 250 hPa (m/s)

(d)

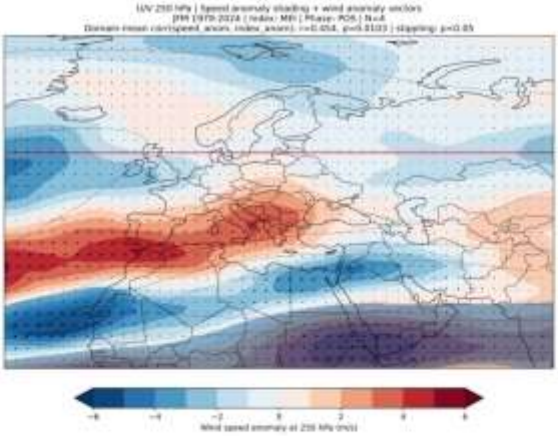
U/V 250 hPa | Speed anomaly shading + wind anomaly vectors
−6
−4
−2
0
2
4
6
Wind speed anomaly at 250 hPa (m/s)

(e)

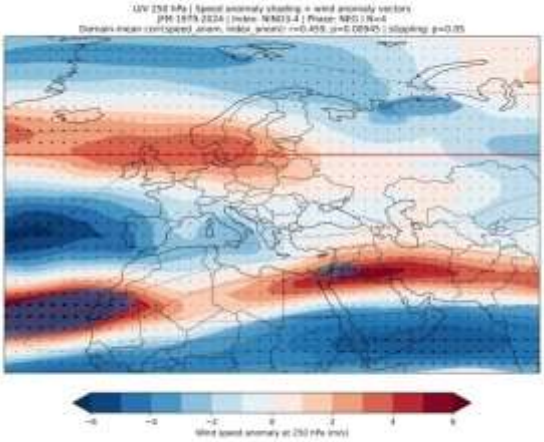
U/V 250 hPa | Speed anomaly shading + wind anomaly vectors
−6
−4
−2
0
2
4
6
Wind speed anomaly at 250 hPa (m/s)

(f)

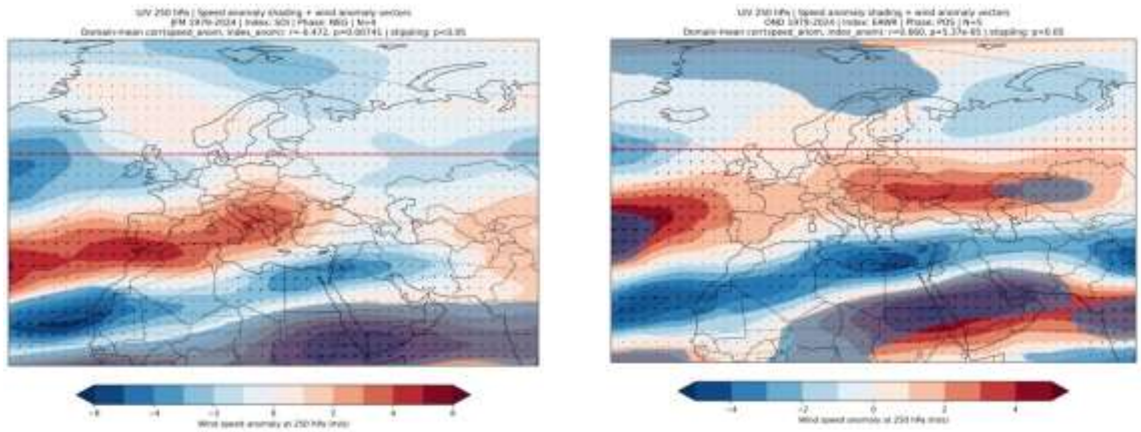

(g) (h)

Figure 8. The Composite seasonal wind speed anomalies of 250 (hPa) Level at different indices.

3-7. The Analysis 500 (Z) Level

3-7-1. Why Z500 is a defensible diagnostic for precipitation extremes

The 500-hPa geopotential height field (Z500) is a fundamental diagnostic in extreme-precipitation analysis because it encapsulates synoptic- to planetary-scale wave structure governing upper-level divergence, quasi-geostrophic (QG) ascent, and cyclone steering. Over Iran and the broader Middle East, extreme rainfall typically coincides with either (i) a pronounced mid-tropospheric trough accompanied by jet-streak forcing over or upstream of the region, or (ii) a quasi-stationary ridge–trough or blocking configuration that prolongs ascent and moisture convergence. Although Z500 alone does not resolve the full moisture budget—requiring complementary diagnostics such as integrated vapor transport, humidity, and vertical velocity—it provides a first-order dynamical framework for assessing whether the atmosphere is predisposed toward sustained uplift or subsidence.

3-7-2. Figure-reading protocol and caveats

The maps show Z500 anomalies (shading; dam) with mean Z500 contours (every 3 dam). Stippling denotes grid points where the reported correlation is significant at $p<0.05$. Each panel also reports a domain-mean correlation coefficient (r) and its p-value, which we interpret as a compact summary of the circulation–extremes linkage strength for the target domain and season. Because sample sizes are modest ($N\approx5$–8), statistical power is limited; therefore, non-significant composites should be read as “suggestive flow regimes” rather than deterministic causal signatures. In other words, neither a visually coherent wave train nor a physically plausible ridge–trough pattern guarantees robust predictability in the statistical sense, and thus inference must balance dynamics against uncertainty.

3-7-3. Seasonal interpretation: AMJ (spring–early summer)

Across AMJ, North Atlantic–Eurasian modes (AMO and EAWR) exhibit the clearest mid-tropospheric (500 hPa) imprint over the Mediterranean–Southwest Asia sector. Their influence is dynamically consistent with Rossby-wave modulation of the subtropical jet and downstream trough positioning. When the upstream waveguide organizes into a ridge–trough configuration that places Iran beneath a downstream trough, Z500 anomalies become negative, enhancing cyclonic vorticity, upper-level divergence, and conditional instability. Under sufficient moisture supply from the Mediterranean, Red Sea, or Arabian Sea pathways, this circulation state favors extreme precipitation. Conversely, ridge dominance suppresses ascent and limits storm development. The AMO+ composite (Figure 9a) shows a statistically robust domain-mean association ($r\approx0.61$, $p<0.01$) and coherent negative height anomalies across Southwest Asia, consistent with enhanced baroclinic development. EAWR− (Figure 9b) similarly exhibits strong domain-mean coupling ($r\approx-0.62$, $p<0.01$), reflecting a large-scale Atlantic–Eurasian wave train that depresses geopotential heights toward the Middle East. Such configurations align with established Euro-Atlantic teleconnection dynamics documented in previous studies (e.g., Atif et al., 2020; Shirvani et al., 2023), which identify trough amplification and jet re-alignment as key mechanisms linking Atlantic variability to West Asian precipitation extremes. By contrast, AMJ ENSO-related composites (Niño-3.4− and SOI−; Figure 9 c–d) display weak and statistically insignificant domain-mean correlations. This suggests that, for spring extremes over Iran, ENSO influence is secondary to Atlantic–Eurasian modes, consistent with prior findings that ENSO impacts are seasonally dependent and often stronger in winter than in late spring. Therefore, the dominant dynamical pathway in AMJ appears to operate through Atlantic-sector wave-train modulation rather than direct tropical Pacific forcing.

Overall, the results indicate that extreme spring precipitation over Iran is most strongly conditioned by mid-tropospheric height anomalies associated with Atlantic–Eurasian teleconnections, which modulate jet positioning, baroclinic growth, and moisture-flux convergence over the region.

3-7-4. Seasonal interpretation: JFM (winter)

In JFM, the composites remain dynamically interpretable but quantitatively weaker. Several panels exhibit a recognizable ridge–trough configuration across the North Atlantic–Europe–Eurasia waveguide; however, domain-mean correlations are small and most p-values are not statistically significant. This apparent mismatch between visually coherent circulation structures and weak domain-mean statistics is physically explicable rather than contradictory. Winter circulation over West Asia is highly energetic, characterized by strong baroclinicity, pronounced jet-latitude fluctuations, and substantial synoptic variability. Under such conditions, the same teleconnection phase can project onto different regional precipitation outcomes depending on longitudinal wave phasing, jet-streak positioning, and the availability of Mediterranean, Red Sea, or Arabian Sea moisture. Thus, a mid-tropospheric trough may enhance extremes when moisture transport and upper-level divergence co-align, yet produce cold–dry anomalies if moisture pathways are suppressed. The rainfall response is therefore dynamically conditional rather than sign-deterministic. EAWR+ (Figure 10a) is the closest to statistical relevance (p≈0.087), suggesting a potential modulation of storm-track curvature toward Southwest Asia. Although marginal, this signal is dynamically plausible: the EAWR phase reorganizes the Eurasian waveguide and can increase blocking frequency and jet waviness, thereby altering cyclone track density over the eastern Mediterranean (Johnson et al., 2024; de Vries et al., 2024). In such a framework, EAWR does not act as a single forcing template; rather, it shifts the probability distribution of synoptic configurations conducive to ascent over Iran.

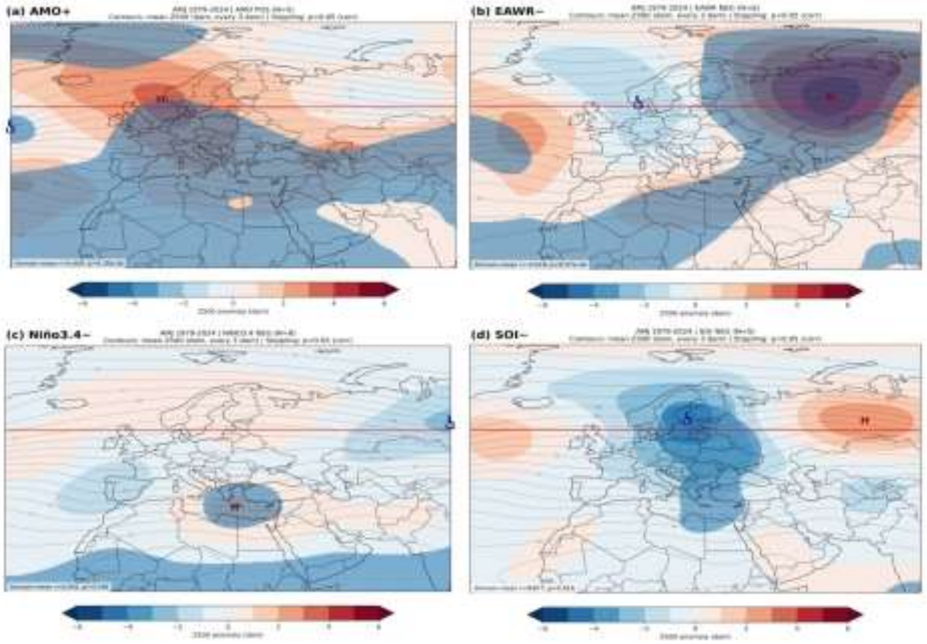

Figure 9. 500 hPa Composite with different Teleconnections (AMJ Seasonal) (1979-2024).

The ENSO proxies (Niño3.4±, ONI−, SOI+; Figure 10 b–e) display near-null domain-mean correlations. This outcome may reflect (i) a genuinely weak contemporaneous ENSO imprint during mid-winter over this sector, (ii) sensitivity to seasonal timing and lag structure—since ENSO teleconnections often peak in OND or late winter—or (iii) sampling limitations. Importantly, ENSO influences over Iran and the broader Middle East are known to weaken from December onward as regional climate variability becomes increasingly governed by the interaction of multiple extratropical teleconnections and internal storm-track dynamics. In other words, tropical forcing may establish the background circulation state in early winter, but subsequent precipitation realization depends more strongly on Euro-Atlantic wave interactions and transient eddy behavior. From an applied perspective, the JFM results imply that winter predictability of extremes based solely on single teleconnection indices is limited. However, the composites still provide diagnostic value: they constrain the set of mid-tropospheric regimes under which extremes are dynamically feasible. Practically, this suggests that seasonal outlooks for Iran should incorporate multi-index monitoring (ENSO family, EAWR, and AO) and explicitly assess jet-stream geometry and moisture-flux diagnostics rather than relying on a single SST-based predictor. Thus, while JFM teleconnection–precipitation linkages are statistically weaker than in SON or MAM, they remain dynamically interpretable within a conditional, multi-driver framework.

3-7-5. Seasonal interpretation: OND (autumn)

The OND MEI+ composite (Figure 11) suggests a modestly wavier, more meridional large-scale flow, but the domain-mean linkage is not significant (p≈0.27). Autumn is a transitional season in which the subtropical jet and the midlatitude storm track are re-organizing; consequently, the same MEI state can coincide with either developing Mediterranean storminess or relatively zonal flow, depending on the concurrent Atlantic–Eurasian configuration. Likewise, the MEI panel should be treated as a hypothesis generator: it indicates what the mid-troposphere looks like in the sampled extreme set, but it does not, by itself, prove that MEI is a reliable driver (Horan *et al.*, 2024; Asadi-Rahim Beygi et al., 2025; Naidu et al., 2020; Singh et al., 2014; Govardhan et al.,2025).

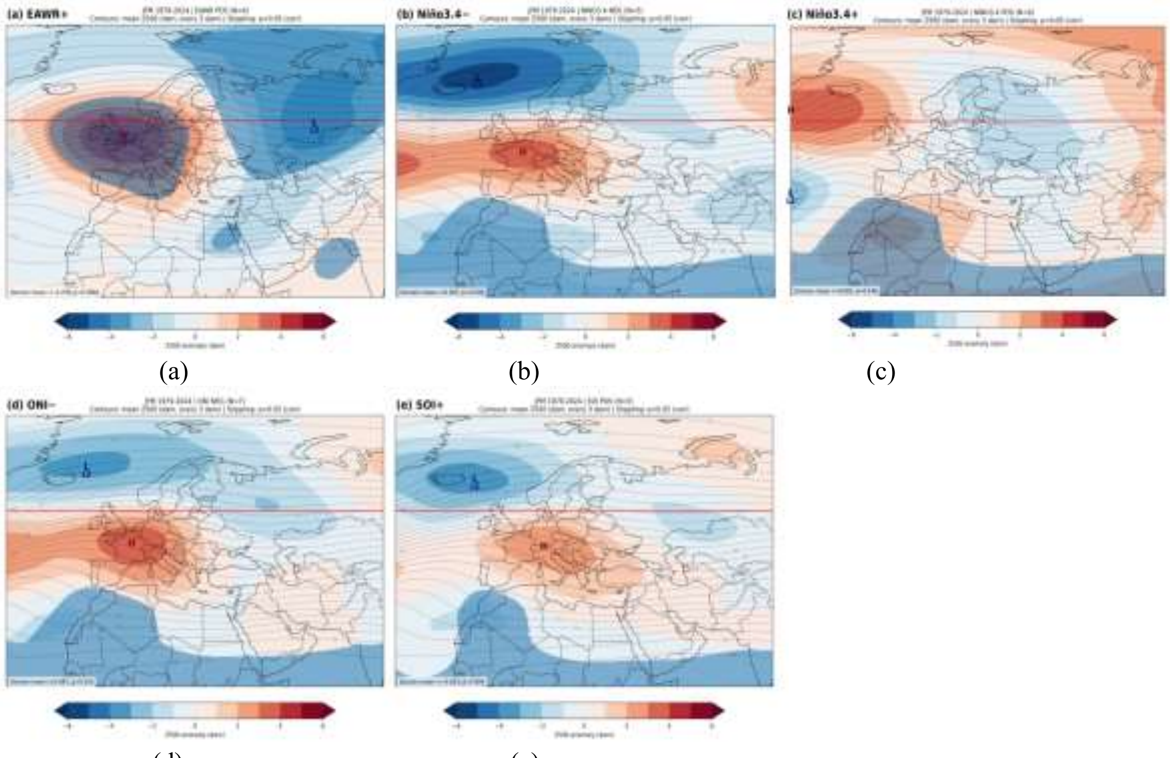

(a) (b) (c)

(d) (e)

Figure 10. JFM Z500 composites (1979–2024): (a) EAWR+, (b) Niño3.4−, (c) Niño3.4+, (d) ONI−, (e) SOI+.

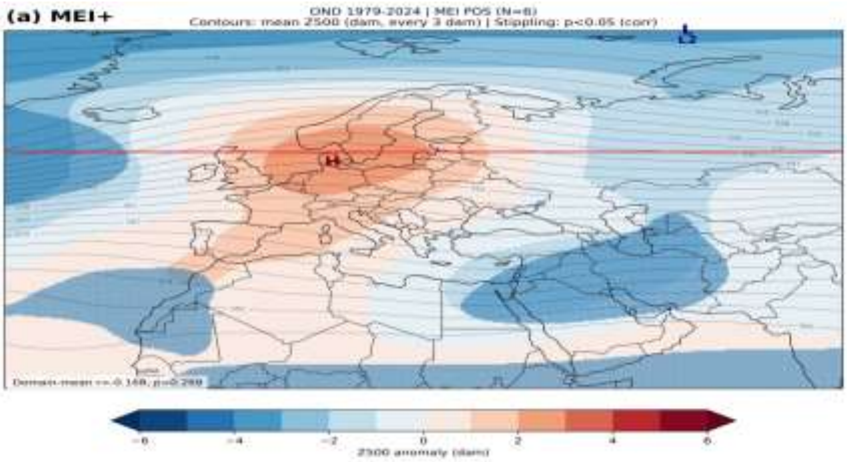

Figure11. OND Z500 composite (1979–2024): MEI+.

In the final stage, the precipitation anomalies of the study region are investigated.

3-8. Seasonal Precipitation-Anomaly Composites (1979–2024) Teleconnection-Conditioned Diagnostics for the Euro–Mediterranean–Middle East Sector

3-8-1. Overview

Figure 13 presents seasonal composites of precipitation anomalies (mm/day) for 1979–2024 conditioned on teleconnection phase (POS/NEG) and sample size (N). Blue (red) shading denotes drier (wetter) conditions relative to climatology. Stippling marks grid cells significant at $p < 0.05$, although spatial autocorrelation implies that isolated significant pixels should be interpreted cautiously. While the header reports domain-mean correlation (r), interpretation emphasizes coherent regional structures rather than the spatial mean alone.

3-8-2. AMJ (April–May–June)

In AMJ, teleconnection signals are comparatively weak and spatially fragmented, consistent with the seasonal retreat of the storm track and increasing influence of land–atmosphere coupling. AMO− (Figure 13a) shows patchy anomalies with modest drying tendencies over parts of Iran and the eastern Mediterranean, though domain-mean associations are weak. EAWR+ (Figure 13b) introduces a north–south contrast, with relatively wetter tendencies over segments of the eastern Mediterranean–Middle East corridor, suggesting wave-train modulation of synoptic steering. NINO3.4− (Figure 13c) leans toward suppressed precipitation across much of the eastern Mediterranean and Iran, indicating that La Niña–like conditions may modestly reduce spring rainfall. Overall, AMJ composites suggest conditional teleconnection influence rather than a dominant forcing mode (Bahrami et al., 2021; Nuroozi et al., 2025).

3-8-3. JFM (January–February–March)

Winter exhibits the clearest and most spatially coherent teleconnection imprint, consistent with a strengthened subtropical jet and active Mediterranean cyclogenesis. AMO− (Figure 13d) corresponds to broadly wetter conditions over segments of the eastern Mediterranean–Iran sector, supporting the role of Atlantic multidecadal variability in modulating downstream circulation. ENSO-related indices (MEI−, NINO3.4−, ONI−; Figures 13 e–g) consistently indicate suppressed winter precipitation across the Mediterranean–Turkey–Iran corridor, while NINO3.4+ (Figure 13h) reverses the signal toward near-normal to wetter conditions over Iran. The phase symmetry across multiple ENSO diagnostics strengthens confidence that the mechanism operates primarily through dynamical jet and storm-track modulation rather than local thermodynamic effects. Thus, JFM represents the season of strongest teleconnection leverage over Iran (Amini et al., 2020; Mishonov et al., 2024).

3-8-4. OND (October–November–December)

OND reflects a transitional regime where both Atlantic and ENSO influences are detectable. EAWR− (Figure 13i) produces a pronounced east–west contrast, with reduced precipitation across Iran coinciding with enhanced activity over parts of Europe, consistent with a displaced storm track. MEI+ (Figure 13j) displays one of the strongest and most coherent positive anomalies over Iran, indicating that ENSO-positive conditions can substantially enhance autumn rainfall. Given the relatively large domain-mean correlation, this panel represents a key result for seasonal predictability.

3-8-5. Cross-panel synthesis focused on Iran

Cross seasons, teleconnection sensitivity over Iran evolves markedly. ENSO-family indices show the most internally consistent behavior: negative phases suppress winter rainfall, whereas positive phases enhance precipitation in JFM and especially OND. AMO and EAWR exert additional influence, primarily by conditioning the background circulation and altering storm-track positioning, thereby modulating whether ENSO forcing projects efficiently onto the region. In summary, teleconnection impacts are strongest in winter, moderate in autumn, and comparatively weak in late spring, reflecting seasonal changes in jet dynamics and synoptic forcing efficiency (Amini, et al., 2020; Bahrami, et al., 2021; Brogli, et al., 2019; Lledó, et al., 2020; Mishonov, et al., 2024; Pour, et al., 2020; Tatli, 2025; Zhang, et al., 2019).

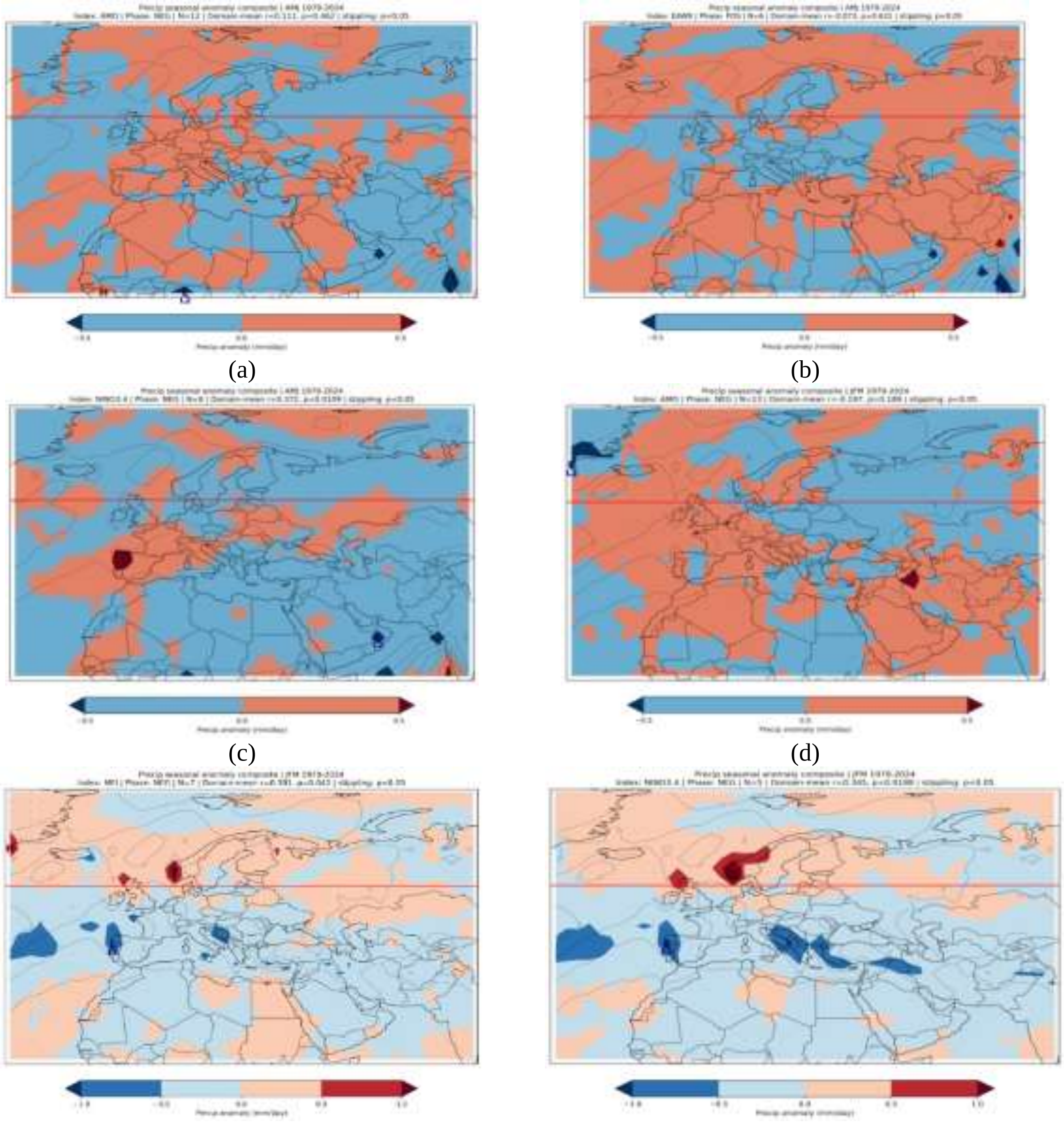

(a)

(b)

(c)

(d)

(e)

(f)

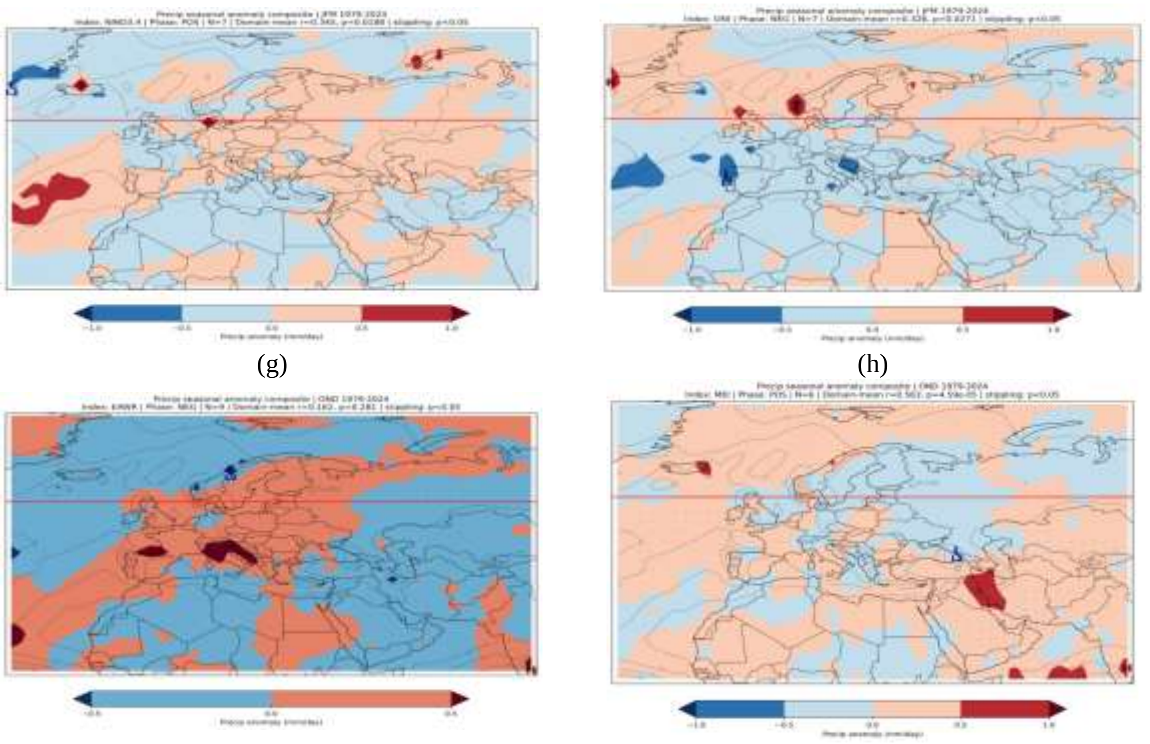

(g) (h)

(i) j

Figure 13. Precipitation anomaly with different teleconnections in different season.

4. Conclusion

This study delivers a quantitatively rigorous and process-consistent synthesis of how largescale ocean–atmosphere teleconnections regulate extreme precipitation across Iran. By integrating daily observations from 160 synoptic stations (1979–2024), hydro-climatic regionalization into five coherent clusters, and a causal discovery framework (PCMCI+), the analysis moves beyond pairwise correlation toward a network-based understanding of directional and lagged influences. The results demonstrate that extreme precipitation variability over Iran is structured by an organized hierarchy of interacting teleconnections operating primarily at seasonal to interannual time scales. Causal-network diagnostics reveal a clear structural asymmetry between drivers and responses: teleconnection nodes exhibit substantially higher mean total degree (≈19.3 ± 10.2) and betweenness centrality (≈0.07 ± 0.08) than precipitation nodes, confirming their role as dynamically central backbone modes rather than passive correlates. ENSO-related indices collectively account for approximately 60–65% of the aggregated absolute causal strength over southern Iran, with Niño-3.4, ONI, MEI, and SOI consistently ranking among the dominant contributors. The Indian Ocean Dipole explains on the order of 13%, while EAWR contributes about 10% and emerges as a seasonally concentrated winter control. Among precipitation metrics, short-duration intensity indices (Rx1day and Rx5day) capture more than one-third of the total teleconnection signal, whereas frequency-based metrics (e.g., R10mm) display weaker and more diffuse connectivity. Robust links concentrate in SON and MAM, while JJA remains largely disconnected, underscoring strong seasonal non-stationarity. Dynamically, these quantitative findings are physically coherent. Teleconnections modulate Iranian extremes by reorganizing subtropical and mid-latitude jet structure, altering Rossby-wave phase alignment, and conditioning mid-tropospheric humidity fields. When jet entrance/exit regions, upper-level divergence maxima, and moisture pathways from the Mediterranean, Red Sea, or Arabian Sea align constructively, short-duration high-impact rainfall becomes more probable. Conversely, misalignment yields suppressed or dry responses. Thus, the teleconnection–precipitation linkage is conditional and circulation-mediated rather than thermodynamically deterministic.

Importantly, the combined network and

composite evidence indicates that teleconnection impacts are regionally heterogeneous and seasonally selective, with the most coherent responses occurring over the Caspian–Alborz and southern clusters during autumn and spring. Winter (JFM) signals remain dynamically interpretable but statistically weaker, highlighting the increased role of internal storm-track variability and multi-mode interference during peak baroclinic activity. From an applied standpoint, three implications follow. First, seasonal forecasting of Iranian precipitation extremes should prioritize ENSO-family diagnostics and IOD states, particularly for anticipating short-duration, high-impact rainfall events. Second, climate-model evaluation should extend beyond mean precipitation bias assessment and explicitly test whether models reproduce the observed causal hierarchy, node centrality structure, and seasonal symmetry of teleconnection influence. Third, future work should expand the causal framework to longer lags, additional tropospheric levels, and land–atmosphere feedback pathways to better quantify memory processes and compound extreme risk.

Overall, the findings establish that extreme precipitation over Iran is not governed by isolated climate modes but by a structured, seasonally evolving teleconnection network. By combining regional clustering with causal discovery, this study provides a process-based benchmark for diagnosing predictability, evaluating climate simulations, and interpreting non-stationary teleconnection behavior in a climatically sensitive transition zone

References

Abid, M. A., Ashfaq, M., Kucharski, F., Evans, K. J., &Almazroui, M. (2020). Tropical Indian Ocean mediates ENSO influence over Central Southwest Asia during the wet season. *Geophysical Research Letters,* 47(18), e2020GL089308.https://doi.org/10.1029/2020GL089308

Afsari, R., Nazari-Sharabian, M., Hosseini, A., &Karakouzian, M. (2024). Projected climate change impacts on the number of dry days and very heavy precipitation days by century's end: A case study of Iran's metropolises. *Water,* 16(16), 2226. https://doi.org/10.3390/w16162226

Aghelpour, P., Bahrami Pichaghchi, H., Varshavian, V., & NoroozValashedi, R. (2023). Evaluating the predictability of eight atmospheric–oceanic signals affecting Iran's droughts, employing intelligence-based and stochastic methods. *Advances in Space Research,* 71(5), 2394–2415. https://doi.org/10.1016/j.asr.2022.10.047

Amini, M., Ghadami, M., Fathian, F., & Modarres, R. (2020). Teleconnections between oceanic–atmospheric indices and drought over Iran using quantile regressions. *Hydrological Sciences Journal,* 65(13), 2286-2295.https://doi.org/10.1080/02626667.2020.1802029

An, X., Chen, W., Fu, S., Hu, P., Li, C., & Sheng, L. (2022). Possible dynamic mechanisms of high-and low-latitude wave trains over Eurasia and their impacts on air pollution over the North China Plain in early winter. *Journal of Geophysical Research: Atmospheres,* 127(13), e2022JD036732.https://doi.org/10.1029/2022JD036732

Asadi-RahimBeygi, N., Mofidi, A., Zarrin, A., & Dadashi-Roudbari, A. (2025). Near-term climate extremes in Iran based on compound hazards analysis. *Scientific Reports,* 15(1), 43843.

Atif, R. M., Almazroui, M., Saeed, S., Abid, M. A., Islam, M. N., & Ismail, M. (2020). Extreme precipitation events over Saudi Arabia during the wet season and their associated teleconnections. *Atmospheric Research,* 231, 104655. https://doi.org/10.1016/j.atmosres.2019.104655

Bahrami, F., Saadatabadi, A. R., Krakauer, N. Y., Mesbahzadeh, T., &Sardoo, F. S. (2021). Synoptic–dynamic patterns affecting Iran's autumn precipitation during ENSO phase transitions. *Climate,* 9(7), 106. https://doi.org/10.3390/cli9070106

Brogli, R., Sørland, S. L., Kröner, N., & Schär, C. (2019). Causes of future Mediterranean precipitation decline depend on the season. *Environmental Research Letters,* 14(11), 114017.https://doi.org/10.1088/1748-9326/ab4438

Dehghani, M., Salehi, S., Mosavi, A., Nabipour, N., Shamshirband, S., & Ghamisi, P. (2020). Spatial analysis of seasonal precipitation over Iran: Co-variation with climate indices. *ISPRS International Journal of Geo-Information,* 9(2), 73. https://doi.org/10.3390/ijgi9020073

De Vries, A. J., Armon, M., Klingmüller, K., Portmann, R., Röthlisberger, M., & Domeisen, D. I. (2024). Breaking Rossby waves drive extreme precipitation in the world's arid regions. *Communications Earth & Environment,* 5(1), 493. https://doi.org/10.1038/s43247-024-01633-y

Ehsan, M. A., Nicolì, D., Kucharski, F., Almazroui, M., Tippett, M. K., Bellucci, A., ... & Kang, I. S. (2020). Atlantic Ocean influence on Middle East summer surface air temperature. *NPJ Climate and Atmospheric Science,* 3(1), 5. https://doi.org/10.1038/s41612-020-0109-1

Esmaeilpour, M., Ghasemi, A. R., Khoramabadi, F., & Rashedi, S. (2021). Spatiotemporal variability of trend in extreme precipitations using fuzzy clustering over Northwest Iran. *Earth Science Informatics,* 14(4), 2123-2132. https://doi.org/10.1007/s12145-021-00680-9

Fan, J., Meng, J., Ludescher, J., Li, Z., Surovyatkina, E., Chen, X., ... & Schellnhuber, H. J. (2022). Network-based approach and climate change benefits for forecasting the amount of Indian monsoon rainfall. *Journal of Climate,* 35(3), 1009-1020. https://doi.org/10.1175/JCLI-D-21-0063.1

Galytska, E., Weigel, K., Handorf, D., Jaiser, R., Köhler, M., Runge, J., & Eyring, V. (2023). Evaluating causal Arctic–midlatitude teleconnections in CMIP6. Journal of Geophysical Research: *Atmospheres,* 128(17), e2022JD037978. https://doi.org/10.1029/2022JD037978

Glantz, M. H., & Ramirez, I. J. (2020). Reviewing the Oceanic Niño Index (ONI) to enhance societal readiness for El Niño's impacts. *International Journal of Disaster Risk Science,* 11(3), 394-403. https://doi.org/10.1007/s13753-020-00275-w

Gong, C., Zhang, C., Yao, D., Bi, J., Li, W., & Xu, Y. (2024). Causal discovery from temporal data: An overview and new perspectives. *ACM Computing Surveys,* 57(4), 1-38. https://doi.org/10.1145/3705297

Govardhan, D., Pathak, R., Ashok, K., Asiri, M. I., Zamreeq, A., & Hoteit, I. (2025). Midlatitude circulations linked to seasonal extreme precipitation and extreme temperature events in the Arabian Peninsula. *Climate Dynamics,* 63(2), 117. https://doi.org/10.1007/s00382-025-07592-0

Haas, M., Goswami, B., & von Luxburg, U. (2023). Pitfalls of climate network construction—a statistical perspective. *Journal of Climate,* 36(10), 3321-3342. https://doi.org/10.1175/JCLI-D-22-0549.1

Hersbach, H., Bell, B., Berrisford, P., Hirahara, S., Horányi, A., Muñoz-Sabater, J., ... & Thépaut, J. N. (2020). The ERA5 global reanalysis. *Quarterly journal of the royal meteorological society,* 146(730), 1999-2049. https://doi.org/10.1002/qj.3803

Horan, M. F., Kucharski, F., Johnson, N., & Ashfaq, M. (2024). Winter precipitation predictability in Central Southwest Asia and its representation in seasonal forecast systems. *npj Climate and Atmospheric Science,* 7(1), 80. https://doi.org/10.1038/s41612-024-00594-5

Hussain, A., Hussain, I., Ali, S., Ullah, W., Khan, F., Rezaei, A., Ullah, S., Abbas, H., Manzoor, A., Cao, J., & Zhou, J. (2023). Assessment of precipitation extremes and their association with NDVI, monsoon and oceanic indices over Pakistan. *Atmospheric Research*, 292, 106873. https://doi.org/10.1016/j.atmosres.2023.106873

IPCC. (2021). Climate Change 2021: The Physical Science Basis. Contribution of Working Group I to the Sixth Assessment Report of the Intergovernmental Panel on Climate Change. *Cambridge University Press.* https://doi.org/10.1017/9781009157896

Jamshidi Khezeli, T., Ranjbar Saadat Abadi, A., Nasr-Esfahany, M. A., Tajbakhsh Mosalman, S., & Mohebalhojeh, A. R. (2022). Autumn and winter extreme precipitation events and their relationship with ENSO, NAO and MJO phases over the west of Iran. *Journal of the Earth and Space Physics,* 47(4), 201–218. https://doi.org/10.22059/jesphys.2021.316961.1007280

Jiménez-Esteve, B., & Domeisen, D. I. (2020). Nonlinearity in the tropospheric pathway of ENSO to the North Atlantic. *Weather and Climate Dynamics,* 1(1), 225-245. https://doi.org/10.5194/wcd-1-225-2020

Kohler, J., Wunderling, N., Donges, J. F., & Vollmer, J. (2021). Complex networks of interacting stochastic tipping elements: Cooperativity of phase separation in the large-system limit. *arXiv preprint arXiv:2104. 09299.* doi.org/10.48550/arXiv.2104.09299

Krich, C., Runge, J., Miralles, D. G., Migliavacca, M., Perez-Priego, O., El-Madany, T., ... & Mahecha, M. D. (2020). Estimating causal networks in biosphere–atmosphere interaction with the PCMCI approach. *Biogeosciences,* 17(4), 1033-1061. https://doi.org/10.5194/bg-17-1033-2020

Kuai, H., Yu, P., Liu, W., Zhang, Y., & Fan, J. (2023). Climate network analysis detects hot spots under anthropogenic *climate change. Atmosphere,* 14(4), 692. https://doi.org/10.3390/atmos14040692

Lemus-Canovas, M. (2022). Changes in compound monthly precipitation and temperature extremes and their relationship with teleconnection patterns in the Mediterranean. *Journal of Hydrology,* 608, 127580. https://doi.org/10.1016/j.jhydrol.2022.127580

L'Heureux, M. L., Tippett, M. K., Wheeler, M. C., Nguyen, H., Narsey, S., Johnson, N., ... & Di Liberto, T. (2024). A relative sea surface temperature index for classifying ENSO events in a changing climate. *Journal of climate,* 37(4), 1197-1211. https://doi.org/10.1175/JCLI-D-23-0406.s1.

Lledó, L., Cionni, I., Torralba, V., Bretonniere, P. A., & Samso, M. (2020). Seasonal prediction of Euro-Atlantic teleconnections from multiple systems. *Environmental Research Letters,* 15(7), 074009. https://doi.org/10.1088/1748-9326/ab87d2

Liu, T., Chen, D., Yang, L., Meng, J., Wang, Z., Ludescher, J., & Schellnhuber, H. J. (2023). Teleconnections among tipping elements in the Earth system. *Nature Climate Change,* 13(1), 67-74. https://doi.org/10.1038/s41558-022-01558-4

Luo, B., Luo, D., Zhuo, W., Xiao, C., Dai, A., Simmonds, I., & Gong, T. (2023). Increased summer European heatwaves in recent decades: Contributions from greenhouse gases-induced warming and Atlantic Multidecadal Oscillation-like variations. *Earth's Future,* 11(8), e2023EF003701. https://doi.org/10.1029/2023EF003701

Mahbod, M., Mashayekhi, S., Rafiee, M. R., & Parnian, A. (2023). Spatio-temporal variations of wet and dry spells in Iran and their association with large-scale climatic indices. *International Journal of Climatology,* 43(6), 2754–2775. https://doi.org/10.1002/joc.8000

Manney, G. L., Hegglin, M. I., & Lawrence, Z. D. (2021). Seasonal and regional signatures of ENSO in upper tropospheric jet characteristics from reanalyses. *Journal of Climate,* 34(22), 9181-9200. https://doi.org/10.1175/JCLI-D-20-0947.s1.

Marshall, G. J. (2021). Decadal variability in the impact of atmospheric circulation patterns on the winter climate of northern Russia. *Journal of Climate*, 34(3), 1005-1021.https://doi.org/10.1175/JCLI-D-20-0566.s1.

Mathbout, S., Lopez-Bustins, J. A., Royé, D., Martin-Vide, J., & Benhamrouche, A. (2020). Spatiotemporal variability of daily precipitation concentration and its relationship to teleconnection patterns over the Mediterranean during 1975–2015. *International Journal of Climatology,* 40(3), 1435-1455. https://doi.org/10.1002/joc.6278

Meshcheryakova, N., & Shvydun, S. (2024). A comparative analysis of centrality measures in complex networks. *Automation and Remote Control,* 85(8), 685-695. https://doi.org/10.1134/S0005117924700127

Miersch, P., Müller, M., Tubbesing, F., Runge, J., Merz, B., & Kemter, M. (2025). Evaluating the robustness of PCMCI+ for causal discovery of flood drivers under complex data characteristics. *Artificial Intelligence for the Earth Systems,* 4(1), e240067. https://doi.org/10.1175/AIES-D-24-0114.1

Mishonov, A., Seidov, D., & Reagan, J. (2024). Revisiting the multidecadal variability of North Atlantic Ocean circulation and climate. *Frontiers in Marine Science,* 11, 1345426.

Naidu, P. D., Ganeshram, R., Bollasina, M. A., Panmei, C., Nürnberg, D., & Donges, J. F. (2020). Coherent response of the Indian Monsoon Rainfall to Atlantic Multi-decadal Variability over the last 2000 years. *Scientific Reports,* 10(1), 1302. https://doi.org/10.1038/s41598-020-58265-3

Ntawuruhunga, D., Ngowi, E. E., Mangi, H. O., Salanga, R. J., & Leonard, K. L. (2025). Contextual drivers of climate-smart agroforestry adoption in Bugesera and Rulindo agroecosystems of Rwanda. Climate Services, 38, 100584. https://doi.org/10.1016/j.cliser.2025.100584

Nuroozi, H., Shirvani, A., & Barlow, M. (2025). The relationship between moisture in the low level of the troposphere and seasonal precipitation over Iran. *Meteorological Applications,* 32(4), e2315. https://doi.org/10.1002/met.70033

Odenweller, A., & Donner, R. V. (2020). Disentangling synchrony from serial dependency in paired-event time series. *Physical Review E,* 101(5), 052213. https://doi.org/10.1103/PhysRevE.101.052213

Pour, S. H., Wahab, A. K. A., & Shahid, S. (2020). Spatiotemporal changes in precipitation indicators related to bioclimate in Iran. *Theoretical & Applied Climatology,* 141. https://doi/org/10.1007/s00704-020-03192-6

Rezaei, A. (2021). Ocean–atmosphere circulation controls on integrated meteorological and agricultural drought over Iran. *Journal of Hydrology,* 603, 126928. https://doi.org/10.1016/j.jhydrol.2021.126928

Runge, J., Gerhardus, A., Varando, G, Eyring, V., & Camps-Valls, G. (2023). Causal inference for time series. *Nature Reviews Earth & Environment,* 4(7), 487–505. https://doi.org/10.1038/s43017-023-00431-y

Saha, R., & Gupte, N. (2023). Signatures of climatic phenomena in climate networks: El Niño and La Niña. *Physical Review E,* 107(6), 064306. https://doi.org/10.1103/PhysRevE.107.064306

Shang, W., Ren, X., Li, S., & Duan, K. (2022). Precursors and formation mechanisms of event-based extreme precipitation during springtime in central-eastern China. *Journal of Climate,* 35(1), 373-385. https://doi.org/10.1175/JCLI-D-20-0884.1

Shirvani, A., Landman, W. A., Barlow, M., & Hoell, A. (2023). Evaluation of the forecast skill of North American Multi-Model Ensemble for monthly and seasonal precipitation forecasts over Iran. https://doi.org/10.1002/joc.7900

Singh, P. K., Mishra, S. K., & Jain, M. K. (2014). A review of the synthetic unit hydrograph: from the empirical UH to advanced geomorphological methods. *Hydrological Sciences Journal,* 59(2), 239-261. https://doi.org/10.1080/02626667.2013.870664

Tatli, H. (2025). Nonlinear precipitation patterns in the Mediterranean and Middle East: insights from ERA5 reanalysis (1940–2024). *Environmental Earth Sciences,* 84(14), 406. https://doi.org/10.1007/s12665-025-12412-z

Tibau, X.-A., Reimers, C., Gerhardus, A., Denzler, J., Eyring, V., & Runge, J. (2022). A spatiotemporal stochastic climate model for benchmarking causal discovery methods for teleconnections. *Environmental Data Science,* 1, e12. https://doi.org/10.1017/eds.2022.11

Toreti, A., Xoplaki, E., Maraun, D., Kuglitsch, F. G., Wanner, H., &Luterbacher, J. (2010). Characterisation of extreme winter precipitation in Mediterranean coastal sites and associated anomalous atmospheric circulation patterns. *Natural Hazards and Earth System Sciences,* 10(5), 1037-1050. https://doi.org/10.5194/nhess-10-1037-2010

Traag, V. A., Waltman, L., & Van Eck, N. J. (2019). From Louvain to Leiden: guaranteeing well-connected communities. *Scientific reports,* 9(1), 1-12. https://doi.org/10.1038/s41598-019-41695-z

Vacca, A. V., Bellomo, K., Fabiano, F., & Von Hardenberg, J. (2025). On the role of AMOC weakening in shaping wintertime Euro-Atlantic atmospheric circulation: A. Vito Vacca et al. *Climate Dynamics,* 63(6), 273. https://doi.org/10.1007/s00382-025-07747-z

Wang, Y., Yin, S., Xiao, Z., Liu, F., Wu, H., Lei, C., Huang, J., & Yang, Q. (2025). Decadal extreme precipitation anomalies and associated multiple large-scale climate driving forces in the Three Gorges Reservoir Area, China. *Water,* 17(4), 477. https://doi.org/10.3390/w17040477

Webb, E. J., & Magi, B. I. (2022). The ensemble oceanic Niño index. *International Journal of Climatology,* 42(10), 5321-5341. https://doi.org/10.1002/joc.7535

West, H., Quinn, N., & Horswell, M. (2022). The influence of the North Atlantic Oscillation and East Atlantic Pattern on drought in British catchments. *Frontiers in Environmental Science,* 10, 754597. https://doi.org/10.3389/fenvs.2022.754597

Zarrin, A., Dadashi-Roudbari, A., & Hassani, S. (2022). Future changes in precipitation extremes over Iran: Insight from a CMIP6 bias-corrected multi-model ensemble. *Pure and Applied Geophysics,* 179(1), 441-464. https://doi.org/10.1007/s00024-021-02904-x

Zhang, R., Sutton, R., Danabasoglu, G., Kwon, Y. O., Marsh, R., Yeager, S. G., & Little, C. M. (2019). A review of the role of the Atlantic meridional overturning circulation in Atlantic multidecadal variability and associated climate impacts. *Reviews of Geophysics,* 57(2), 316-375. https://doi.org/10.1029/2019RG00064

Zhang, T., Hoell, A., Perlwitz, J., Eischeid, J., Murray, D., Hoerling, M., & Hamill, T. M. (2019). Towards probabilistic multivariate ENSO monitoring. *Geophysical Research Letters,* 46(17-18), 10532-10540. https://doi.org/10.1029/2019GL083946

Zhang, Y., Zhou, W., Wang, X., Chen, S., Chen, J., & Li, S. (2022). Indian Ocean Dipole and ENSO's mechanistic importance in modulating the ensuing-summer precipitation over Eastern China. *npj Climate and Atmospheric Science,* 5(1), 48. https://doi.org/10.1038/s41612-022-00271-5